

Contents lists available at ScienceDirect

International Journal of Engineering Science

journal homepage: www.elsevier.com/locate/ijengsci



Full length article

Thermomechanical modeling of functionally graded materials based on bimaterial fundamental solutions

Chunlin Wu ^{a,d}, Liangliang Zhang ^b, George J. Weng ^c, Huiming Yin ^{d,*}

- ^a Shanghai Institute of Applied Mathematics and Mechanics, School of Mechanics and Engineering Science, Shanghai University, 99 Shangda Road, Shanghai 200044, China
- ^b Department of Applied Mechanics, China Agricultural University, 17 Qinghua East Road, Beijing, 100083, China
- ^c Department of Mechanical and Aerospace Engineering, Rutgers University, New Brunswick, NJ 08903, United States of America
- d Department of Civil Engineering and Engineering Mechanics, Columbia University, 500 W 120th Street, NY, 10027, United States of America

ARTICLE INFO

Keywords: Fundamental solutions Dual equivalent inclusion method Homogenization Cross-scale modeling Inclusion-based boundary element method (iBEM)

ABSTRACT

The Green's function technique has been used to directly calculate the local fields of a functionally graded material (FGM) under thermomechanical loading, thus predicting its effective material properties. For a bi-phase FGM continuously switching the particle and matrix phases, the particle size and material gradation play a complex role in its effective material behavior. Using Eshelby's equivalent inclusion method, particles are simulated by a source of eigen-fields in a bounded bi-layered domain, while the boundary effects are evaluated by the boundary integrals of the fundamental solutions. Using the volume integral of Green's functions, over 10,000 particles are used to simulate an FGM under thermal and mechanical loading, respectively. The dual equivalent inclusion method is used to solve for the temperature and stress fields coupled with temperature loading. The averaged thermomechanical field distribution in the gradation direction is evaluated under different loading conditions. The effective stiffness, thermal expansion coefficient, and heat conductivity significantly change with the loading condition, particle size, and material gradation. The homogenization methods, which approximate an FGM as a continuously graded material with thermoelastic properties depending on the volume fraction only, cannot capture these micromechanical features of FGMs, while the present cross-scale approach with the inclusion-based boundary element method (iBEM) directly evaluates local fields and predicts effective material behaviors with high fidelity and efficiency.

1. Introduction

Advanced material designs are often subjected to requirements in multi-functions with a number of constraints, which may not be achieved by conventional composites with uniform particle distributions (Saleh et al., 2020; Wang et al., 2019). Functionally graded materials (FGMs) have been used in many engineering industries, such as biomedical (Roy, 2020), aerospace (Kumar et al., 2013), and automobile (Ram et al., 2017) applications, in which materials gradually change from one phase to another in the gradation direction. With the graded microstructure, FGMs exhibit the improved integrity and performance of the material systems (Carvalho et al., 2015; Tanvir et al., 2017).

In the transition of the material phases, the material concentration variation in the gradation direction can be either step functions or continuous functions. An FGM with a step function of material phase distribution is equivalent to laminated composites, which

E-mail addresses: chunlinwu@shu.edu.cn (C. Wu), llzhang@cau.edu.cn (L. Zhang), gjweng@soe.rutgers.edu (G.J. Weng), yin@civil.columbia.edu (H. Yin).

https://doi.org/10.1016/j.ijengsci.2024.104040

Received 16 October 2023; Received in revised form 3 February 2024; Accepted 10 February 2024 Available online 20 February 2024 0020-7225/© 2024 Elsevier Ltd. All rights reserved.



^{*} Corresponding author.

may still exhibit discontinuous properties at interfaces between layers, i.e., thermal expansion ratio and stiffness, which arises concentration of misfit stress and thermal stress due to large temperature variation (Kumar et al., 2013) and thus causes damage and separation of layers (Lin et al., 2017). A continuous variation of material phases is favorable and allows the application of materials with conflicting properties (Shinohara, 2013). Chawla (2003) presented an example of an aerospace thermo-structure composed of ceramic and polymers. Due to the gradual change of the microstructure, thermal stress in the FGMs can be significantly relieved compared to a bi-layered structure (Yin et al., 2007, 2004).

Because FGMs play important roles in many engineering fields, investigating mechanical and thermomechanical behaviors has attracted extensive attention. Kesler et al. (1998) and Khor and Gu (2000) measured the coefficients of thermal expansion and thermal stress concerning the graded direction. For numerical methods, finite element method (FEM) (Agrawal et al., 2003; Reiter & Dvorak, 1998; Reiter et al., 1997) have been applied to understand and analyze experimental results. Ebrahimijahan et al. (2022) integrated the finite difference approach with radial basis functions for the simulation of two-dimensional FGMs, which aims to reduce the number of grid nodes. Since FGMs possess complex microstructures, the accuracy of numerical methods depends on the discretization of material phases with different shapes and distributions (Yin et al., 2007; Zou & He, 2018). When the particle size varies in a range, using a finite element mesh to describe those particles is difficult. Even if internal grids, meshes, or cells can reasonably simulate the geometry, it is challenging to provide accurate results because of the stress concentration and singularities. Therefore, defining the size of a representative volume element (RVE) or unit cell for homogenization is difficult.

More methods turned to the effective graded material behavior with equivalent material phase variation instead of the actual particle distribution. Aboudi's group (Aboudi et al., 1996a, 1996b) proposed a higher-order theory for FGMs. In the review paper (Aboudi et al., 1999), the authors pointed out that using standard micromechanical models on an RVE for FGMs disobeys the non-unique definition of RVE because of continuously changing material properties along the graded direction and nonuniform spacing of inhomogeneities. In general, the primary purpose of RVE is to homogenize the microscopic features and thus simplify the materials in evaluating effective macroscopic behaviors. For a homogeneous composite with large sizes compared with inhomogeneities, it is suitable to apply RVE based on the rational assumption of an infinite material domain. However, when the gradation and inhomogeneity size of FGMs are not very small for an FGM, an RVE with a different size may provide different results, which may never reach a convergent result.

Due to the above limitations, several numerical methods and their extensions have been proposed to simulate the continuously changing material properties. The conventional FEM with homogeneous elements has been used to simulate two-phase FGMs (Anlas et al., 2000; Fujimoto & Noda, 2004; Reiter & Dvorak, 1998; Reiter et al., 1997). The simulations were achieved by carefully assigning two properties to elements in successive layers, which may lead to stepwise changing properties along the gradation direction. Similarly, the conventional multi-region boundary element method (BEM) can also be used through discretizing internal boundaries. This school of methods can provide rational predictions with refined mesh, but the main obstacles are a trivial preparation process and a large consumption of computational resources. Subsequently, Kim and Paulino (2002) and Santare and Lambros (2000) suggested using a graded finite element, where the material properties can be evaluated through the Gauss points of the element. Using the graded finite element (GFM), Burlayenko et al. (2017) simulated a two-dimensional plane strain FGM plate. Although the GFM avoids the preparation process of assigning material properties by volume fraction, it simply assumes uniform material properties at the same height (layer). It ignores the critical physics of particle interactions, resulting in an unrealistic local field with two strong assumptions. Other related works can be found in the critical review (Jha et al., 2013). Overall, the inhomogeneity interactions with the loading configuration in FGM applications have not been well studied. An actual FGM sample with loading on the boundary may show some actual material behavior across the micro- and macro-scales with both local fields and effective material behavior.

In the recent book (Yin et al., 2022), we presented the algorithm of iBEM, where the boundary response and inhomogeneity interactions are fully considered through BEM and EIM, respectively. Since three-order Taylor series polynomials express the eigenfields on the ellipsoidal inhomogeneities and thus no internal mesh is required, the number of degrees of freedom (DOF) is tailorable and well controlled, which is particularly suitable for virtual experiments of a large number of inhomogeneities. Considering a bi-phase FGM composite with phase concentration continuously changing from 0 to 1 (Fig. 1), it is straightforward to assign inhomogeneities to satisfy gradation distribution. However, similar to the work (Reiter et al., 1997), this scheme is neither physical nor efficient because the particle's volume fraction cannot reach 100%, and the number of inhomogeneities increasing from 0 to 100% results in a large number of particles that lead to high computational costs and physical difficulty to make the particle phase close to 100%. Alternatively, a bi-matrix model for FGM with interchanged inhomogeneity and matrix phases (Fig. 1) will be more reasonable. Considering a linearly graded FGM, the entire volume fractions of inhomogeneities are 50% and 25% for one-matrix and bi-matrix models, respectively, so that the bi-matrix model can significantly reduce the DOFs with a better physical meaning of the particle phase volume fraction much less than 50%, which can be other values depending on the physics of materials.

In the literature, the thermomechanical analysis is generally conducted in two separate steps: (i) solving thermal fields and (ii) coupling temperature-induced stress through the domain integral of the kernel functions. Prasad et al. (1994) mathematically transformed the domain integrals of temperature into boundary integrals with the Galerkin technique, where the kernel function is also known as the thermoelastic fundamental solution. Since then, the thermomechanical analysis can be completed by solving one global matrix instead of two coupling steps. Following Prasad's method, this paper firstly presents a bimaterial BEM based on elastic (Walpole, 1996; Wu, Zhang, Cui & Yin, 2023) and thermoelastic bimaterial fundamental solutions (Hou et al., 2013; Wu, Wang, & Yin, 2023). Since two matrices generally exhibit different thermoelastic properties, the DEIM is proposed to consider thermal and elastic fields (Wu, Wang, & Yin, 2023; Wu, Zhang, Singhatanadgid & and Zhang, 2023). In DEIM, two eigen-fields are used: (i) eigen-temperature gradient (ETG) for mismatch of thermal conductivity and (ii) eigenstrain for mismatch of thermal

One-matrix model Bi-matrix model

Fig. 1. Schematic plot and comparison of one-matrix and bi-matrix models.

modulus and stiffness. Due to pairwise interactions and boundary effects, Taylor's series expansion has been utilized to describe spatial variations of the two eigen-fields. Solving the global system of linear equations, the thermoelastic boundary response and eigen-fields can be determined. Subsequently, thermomechanical fields, i.e., temperature, thermal strain, etc., and the related effective behaviors can be determined through the post-process.

This paper uses the bimaterial fundamental solution to develop a single-domain boundary integral method for thermomechanical simulation of an FGM with two matrix phases containing many particles. Section 2 presents a bi-layered system embedded with multiple inhomogeneities. Subsequently, the bimaterial elastic/thermoelastic fundamental solutions and global matrix of iBEM are presented in Section 3. Subsequently, the accuracy and efficiency of the iBEM algorithm is verified by comparing thermoelastic fields and the computational costs with the FEM results of simple case studies. Section 5 presents numerical examples of ceramic–metal FGMs with different distribution and particle dimensions.

2. Problem statement

Consider a bimaterial containing a number of inhomogeneities, which interchanges material phases of inhomogeneities and matrix in the gradation direction, under a thermomechanical load. It can be formulated by a boundary value problem (BVP) of a two-jointed dissimilar half-spaces \mathcal{D} composed of the upper \mathcal{D}^+ and lower \mathcal{D}^- phases, which is embedded with multiple N_I subdomains Ω^I , where \mathcal{D}^+ , \mathcal{D}^- and Ω^I generally possess dissimilar material properties, which are thermal conductivity (K), modulus (A) and stiffness (C). Let superscripts (.) I , (.) I indicates material properties of \mathcal{D}^+ , \mathcal{D}^- and Ω^I respectively. For a two-phase FGM, the inhomogeneity and matrix switch the properties in the two domains, which is a special case for this general BVP.

Let λ and μ represent the two Lame constants. Then the isotropic stiffness tensor $C_{ijkl} = \lambda \delta_{ij} \delta_{kl} + \mu (\delta_{ik} \delta_{jl} + \delta_{il} \delta_{jk})$ and thermal modulus $\mathcal{A} = (3\lambda + 2\mu)\alpha$ can be expressed. Shown in Fig. 2, a cuboid bi-layered system with length l, width b, thicknesses h_1 and h_2 contains multiple spherical inhomogeneities, which is subjected to prescribed thermal (temperature T, flux \mathbf{q}) and elastic (displacement \mathbf{u} , traction \mathbf{t}) boundary conditions.

The bimaterial interface is placed at the $x_1 - x_2$ plane. In the following, perfect subdomain and bimaterial interfaces are assumed, which exhibit non-debonding behavior and hence satisfy thermal and elastic continuity equations of temperature, flux, displacement, and traction as follows:

$$T(\mathbf{x}^{+}) = T(\mathbf{x}^{-}), \quad q_{i}(\mathbf{x}^{+})n_{i}(\mathbf{x}^{+}) = q_{i}(\mathbf{x}^{-})n_{i}(\mathbf{x}^{-})$$

$$u_{i}(\mathbf{x}^{+}) = u_{i}(\mathbf{x}^{-}), \quad \sigma_{i,i}(\mathbf{x}^{+})n_{i}(\mathbf{x}^{+}) = \sigma_{i,i}(\mathbf{x}^{-})n_{i}(\mathbf{x}^{-})$$
(1)

where superscripts + and – indicate the inward and outward surfaces of bimaterial and subdomain interfaces, respectively; n stands for the unit surface normal vector of interfaces. Combining prescribed boundary conditions and continuity equations at interfaces, the thermal and its induced thermoelastic BVPs can be formulated, usually handled by multi-region schemes and volume integrals. As introduced previously, the thermal effects are mathematically involved through the boundary integral equation of bimaterial thermoelastic fundamental solutions. In addition, the conventional BVPs (inhomogeneity problems) were analytically reformulated to determine eigen-fields, which elegantly avoided trivial discretization procedures of numerical methods. In this paper, the iBEM method employs the bimaterial thermal, thermoelastic, and elastic fundamental solutions to analyze thermoelastic inhomogeneity problems in a bounded bi-layered structure, and it is further applied for thermoelastic case studies of FGM composites.

3. Formulation and algorithm implementation

The above BVP will be formulated with the iBEM (Yin et al., 2022) using the bimaterial fundamental solution instead to achieve the interface continuity analytically.

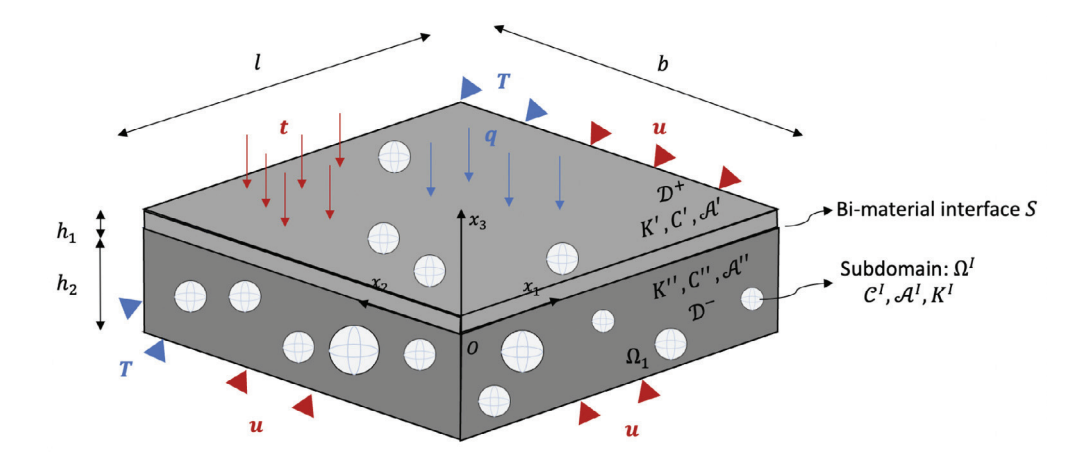


Fig. 2. Illustrative plot of a cuboid bi-layered system embedded with multiple spherical inhomogeneities subjected to prescribed thermomechanical conditions (dimensions: length l, width b, thickness h_1 , h_2).

3.1. Bimaterial fundamental solutions

The fundamental solution provides a response at field point \mathbf{x} caused by a unit excitation at arbitrary source point \mathbf{x}' . For a concentrated heat source $\delta(\mathbf{x}')$, the bimaterial thermal $(G(\mathbf{x}, \mathbf{x}'))$ and thermoelastic $(G_i(\mathbf{x}, \mathbf{x}'))$ fundamental solution provides temperature and displacement, respectively,

$$T(\mathbf{x}) = G(\mathbf{x}, \mathbf{x}')\delta(\mathbf{x}'); \quad u_i(\mathbf{x}) = G_i(\mathbf{x}, \mathbf{x}')\delta(\mathbf{x}')$$
(2)

For a point force f, the bimaterial elastic fundamental solution $G_{ij}(\mathbf{x},\mathbf{x}')$ provides the displacement field,

$$u_i(\mathbf{x}) = G_{ii}(\mathbf{x}, \mathbf{x}') f_i(\mathbf{x}') \tag{3}$$

Though the fundamental solutions are expressed with the same character *G*, they are distinguished through ranks. Although there exist various expressions of bimaterial elastic (Walpole, 1996) and thermoelastic (Wu, Wang, & Yin, 2023) fundamental solutions, in the following, they are modified and present in the form of potential functions, which is particularly suitable for domain integrals in Eshelby's inhomogeneity problem. The derivation of bimaterial fundamental solutions generally involves a method of the image. Therefore, the explicit expressions depend on the relative position of the source and field points.

3.1.1. Thermal fundamental solution

The explicit thermal fundamental solution is provided in our recent work (Wang et al., 2022),

$$G(\mathbf{x}, \mathbf{x}') = \begin{cases} \frac{1}{4\pi K^w} (\phi + \frac{K^w - K^s}{K^w + K^s} \overline{\phi}) & x_3' x_3 \ge 0\\ \frac{1}{2\pi (K^w + K^s)} \phi & x_3' x_3 < 0 \end{cases}$$
(4)

where (i) w=', s='' for $x_3' \ge 0$ and (ii) w='', s=' for $x_3' < 0$; $\psi=|\mathbf{x}-\mathbf{x}'|$ and $\phi=\psi^{-1}$ are the biharmonic and harmonic potential functions, respectively; $\overline{(.)}$ represents image terms, for example, $\overline{\phi}=|\mathbf{x}-\overline{\mathbf{x}}'|^{-1}$, where $\overline{x}_i'=Q_Ix_i'$ and the vector $\mathbf{Q}=(1,1,-1)$. Here the dummy index rule follows Mura's notation (Mura, 1987) that the upper case subscript changes with lower case subscript but not be summed.

3.1.2. Thermoelastic fundamental solution

The explicit thermoelastic fundamental solution is provided in our recent work (Wu, Wang, & Yin, 2023),

$$G_{i}(\mathbf{x}, \mathbf{x}') = \frac{1}{2\mu^{q}} \begin{cases} \mathcal{H}_{5}^{q} \psi_{,i} + (\mathcal{H}_{1}^{q} + L_{B}^{y}) \overline{\beta}_{,i}^{y} + L_{B}^{y} \overline{\psi}_{,i} \\ + x_{3} \left[\chi \left(L_{D}^{y} - L_{F}^{y} \right) \overline{\alpha}_{,i}^{y} + L_{C}^{y} \left(\overline{\psi}_{,i3} + 2(1 - 2\nu^{q}) \delta_{i3} \overline{\phi} - x_{3} \overline{\phi}_{,i} \right) \right] & x_{3} x_{3}' \ge 0 \\ + \delta_{i3} \left[-(3 - 4\nu^{q}) \left(\mathcal{H}_{3}^{q} \overline{\alpha}^{y} + L_{C}^{y} \overline{\psi}_{,3} \right) + \chi \left(4(1 - \nu^{q}) \mathcal{H}_{6}^{q} - L_{B}^{y} \right) \overline{\alpha}^{y} \right] \\ \left(\mathcal{H}_{2}^{q} + L_{G}^{y} \right) \beta_{,i}^{y} - x_{3} \left[\mathcal{H}_{4}^{q} - L_{G}^{y} \right] \alpha_{,i}^{y} + L_{G}^{y} \psi_{,i} \\ - \chi \delta_{i3} \alpha^{t} \left[L_{G}^{y} + (3 - 4\nu^{q}) \mathcal{H}_{4}^{q} - 4(1 - \nu^{q}) \mathcal{H}_{7}^{q} \right] \end{cases}$$

$$(5)$$

where (i) q = ', y = u and $\chi = 1$ for $x_3' \ge 0$ and (ii) q = '', y = l and $\chi = -1$ for $x_3' < 0$. Four branches of harmonic functions (α, β) are listed below,

$$\alpha^{u} = \ln[x'_{3} - x_{3} + \psi], \quad \overline{\alpha}^{u} = \ln[x'_{3} + x_{3} + \overline{\psi}]
\beta^{u} = (x'_{3} - x_{3})\alpha^{u} - \psi, \quad \overline{\beta}^{u} = (x'_{3} + x_{3})\overline{\alpha}^{u} - \overline{\psi}
\alpha^{l} = \ln[-x'_{3} + x_{3} + \psi], \quad \overline{\alpha}^{l} = \ln[-x'_{3} - x_{3} + \overline{\psi}]
\beta^{l} = (-x'_{2} + x_{3})\alpha^{l} - \psi, \quad \overline{\beta}^{l} = (-x'_{2} - x_{3})\overline{\alpha}^{l} - \overline{\psi}$$
(6)

 α and β are Boussinesq's displacement potential functions (Barber, 1992; Boussinesq, 1885), and they are introduced to handle higher order partial derivatives (third direction) in Boussinesq's problem of surface load. The four branches of expressions in Eq. (6) are obtained through partial integration along the third axis and differentiated by 2 integral limits as $[x_3, -\infty)$, $(\infty, x_3]$ for superscript u and u, respectively. For example, $u = \int_{x_3}^{+\infty} \phi(x_1, x_2, t) dt$ and $u = \int_{\infty}^{+\infty} \overline{\phi}(x_1, x_2, t) dt$. The material coefficients u = u are provided as follows:

$$\mathcal{H}_{1}^{u} = \mathcal{H}_{5}^{u} - 2\mu' \left[\frac{\mathcal{H}_{7}^{u}(1 - \nu'')}{(3 - 4\nu'')\mu' + \mu''} + \frac{(\mathcal{H}_{5}^{u} + \mathcal{H}_{6}^{u})(1 - \nu')}{(3 - 4\nu')\mu'' + \mu'} \right]$$

$$\mathcal{H}_{2}^{u} = -2\mu'' \left[\frac{\mathcal{H}_{7}^{u}(1 - \nu'')}{(3 - 4\nu'')\mu' + \mu''} + \frac{(\mathcal{H}_{5}^{u} + \mathcal{H}_{6}^{u})(1 - \nu')}{(3 - 4\nu')\mu'' + \mu''} \right]$$

$$\mathcal{H}_{3}^{u} = \frac{4\mathcal{H}_{6}^{u}(1 - \nu')\mu'' - \mathcal{H}_{5}^{u}(\mu' - \mu'')}{(3 - 4\nu')\mu'' + \mu'}, \quad \mathcal{H}_{4} = 4\mathcal{H}_{7}^{u} \frac{(1 - \nu'')\mu'}{(3 - 4\nu'')\mu' + \mu''}$$

$$\mathcal{H}_{5}^{u} = \frac{1}{8\pi K'} \frac{(1 - 2\nu')\mathcal{A}'}{1 - \nu'}, \quad \mathcal{H}_{6}^{u} = \frac{1}{8\pi K'} \frac{(1 - 2\nu')\mathcal{A}'}{1 - \nu'} \frac{K' - K''}{K' + K''}, \quad \mathcal{H}_{7}^{u} = \frac{1}{4\pi (K' + K'')} \frac{(1 - 2\nu'')\mathcal{A}''}{1 - \nu''}$$

$$L_B^u = \mathcal{H}_5^u \frac{(3 - 4\nu')(\mu' - \mu'')}{(3 - 4\nu')\mu'' + \mu'}, \quad L_C^u = 2\mathcal{H}_5^u \frac{(\mu' - \mu'')}{(3 - 4\nu')\mu'' + \mu'}$$

$$L_D^u = \frac{4\mathcal{H}_6^u (1 - \nu')\mu''}{(3 - 4\nu')\mu'' + \mu'}, \quad L_F^u = \frac{4\mathcal{H}_5^u (\mu' - \mu'')(1 - \nu')}{(3 - 4\nu')\mu'' + \mu'}$$
(8)

Following the same fashion, when the source point is located at \mathcal{D}^- ($x_3' < 0$), material coefficients $\mathcal{H}_1^l \sim \mathcal{H}_7^l$ and $L_B^l \sim L_F^l$ can be obtained through switching sequence of material properties of two matrix phases. For instance, $\mathcal{H}_7^l = \frac{1}{4\pi(K'+K'')}\frac{(1-2V')A'}{1-V'}$.

3.1.3. Elastic fundamental solution

The explicit bimaterial elastic fundamental solution was proposed by Walpole (Walpole, 1996, 1997). Subsequently, the fundamental solution was completed by current authors and implemented in BEM for elastic analysis of bi-layered structures (Wu, Zhang, Cui & Yin, 2023). The compact bimaterial elastic fundamental solution is expressed as Eq. (9),

$$G_{ij}^{y}(\mathbf{x}, \mathbf{x}') = \frac{1}{4\pi\mu^{w}} \begin{cases} (\delta_{ij}\phi - \frac{\psi_{,ij}}{4(1 - \nu^{w})}) + A^{y}\overline{\phi}\delta_{ij} + \chi B^{y}(\delta_{i3}\delta_{jk} - \delta_{ik}\delta_{j3})\overline{\alpha}_{,k}^{y} \\ - C^{y}x_{3} \left[Q_{J}\overline{\psi}_{,ij3} + 4(1 - \nu^{w})\delta_{j3}\overline{\phi}_{,i} + 2(1 - 2\nu^{w})\delta_{i3}Q_{J}\overline{\phi}_{,j} - Q_{J}x_{3}\overline{\phi}_{,ij}\right] & x_{3}'x_{3} \ge 0 \\ - D^{y}Q_{I}Q_{J}\overline{\psi}_{,ji} - (G^{y} + B^{y})Q_{J}\overline{\beta}_{,ij}^{y} \\ (\delta_{ij}\phi - \frac{\psi_{,ij}}{4(1 - \nu^{w})}) + A^{y}\phi\delta_{ij} + \chi B^{y}(\delta_{i3}\delta_{jk} - \delta_{ik}\delta_{j3})\alpha_{,k}^{y} \\ - D^{y}\psi_{,ij} - \chi x_{3}F^{y}\alpha_{,ij}^{y} - (G^{y} + B^{y})Q_{I}\beta_{,ji}^{y} \end{cases}$$

$$(9)$$

where four branches of α and β are expressed in Eq. (6); the material coefficients $A^u \sim G^u$ are listed as Eq. (10),

$$A^{u} = \frac{\mu' - \mu''}{\mu' + \mu''}, \quad B^{u} = \frac{2\mu'(1 - 2\nu')(\mu' - \mu'')}{(\mu' + \mu'')(\mu' + \mu''(3 - 4\nu'))}$$

$$C^{u} = \frac{\mu' - \mu''}{2(1 - \nu')(\mu' + (3 - 4\nu')\mu'')}, \quad D^{u} = \frac{3 - 4\nu'}{2}C^{u}$$

$$F^{u} = \frac{2\mu'(\mu'(1 - 2\nu'') - \mu''(1 - 2\nu'))}{(\mu' + \mu''(3 - 4\nu'))(\mu'' + \mu'(3 - 4\nu''))}$$

$$G^{u} = \frac{\mu'(\mu''(1 - 2\nu'')(3 - 4\nu') - \mu'(1 - 2\nu')(3 - 4\nu''))}{(\mu' + \mu''(3 - 4\nu'))(\mu'' + \mu'(3 - 4\nu''))}$$
(10)

Similar to Section 3.1.2, coefficients $A^l \sim G^l$ can be derived through switching sequences of material properties of two matrix phases. For example, $A^l = \frac{\mu^{\prime\prime\prime} - \mu^{\prime\prime}}{\mu^{\prime} + \mu^{\prime\prime}}$. In general, two matrix phases exhibit different material properties. The bimaterial thermal, thermoelastic and elastic fundamental solutions can be further modified for infinite and semi-infinite problems by tailoring the material constants of one layer equal to the ones of the other layer and zero or infinite, respectively, and the explicit forms are provided in Wu, Wang, and Yin (2023).

3.2. Boundary element method with bimaterial fundamental solution

Proposed in Prasad et al. (1994) for thermoelastic stress intensity analysis, the authors applied Galerkin's stress vector to transform domain integrals as boundary integrals instead. The main advantages are: (i) It overcomes domain integrals of temperature so that no internal cells are required. As a result, the thermal effects are not considered by polynomial interpolation anymore, which reduces errors of approximation; (ii) The solutions of both thermal and thermoelastic problems can be obtained with the same boundary mesh using the collocation method, which retains the strong-form property of BEM. The solving schemes can be constructed as thermal thermoelastic and elastic boundary integral equations.

3.2.1. Bimaterial thermal boundary integral equations

Consider a domain \mathcal{D} composed of two jointed different isotropic homogeneous material phases, which is subjected to prescribed thermal boundary conditions such as temperature T^{BC} and flux \mathbf{q}^{BC} . Notice that only flux perpendicular to the boundary surface is considered, a scalar quantity for boundary response. Based on the concept of fundamental solution, through boundary integral equations of boundary temperature and flux, the temperature field can be obtained as Eq. (11),

$$T^{B}(\mathbf{x}) = -\int_{\partial \mathcal{D}^{T}} K(\mathbf{x}') n_{m} G_{,m'}(\mathbf{x}, \mathbf{x}') T^{BC}(\mathbf{x}') d\mathbf{x}' + \int_{\partial \mathcal{D}^{Q}} G(\mathbf{x}, \mathbf{x}') q^{BC}(\mathbf{x}') d\mathbf{x}'$$

$$\tag{11}$$

where **n** is unit outward surface normal of surface \mathcal{D}^T ; $(.)_{,m'} = \partial x_{m'}(.)$ denotes partial differentiation with respect to source point. Using the Fourier's law, heat flux at field point is as Eq. (12),

$$q_i^B(\mathbf{x}) = K(\mathbf{x}) \left[\int_{\partial D^T} K(\mathbf{x}') n_m G_{,m'i}(\mathbf{x}, \mathbf{x}') T^{BC}(\mathbf{x}') d\mathbf{x}' - \int_{\partial D^Q} G_{,i}(\mathbf{x}, \mathbf{x}') q^{BC}(\mathbf{x}') d\mathbf{x}' \right]$$

$$(12)$$

3.2.2. Bimaterial thermoelastic and elastic boundary integral equations

Following the description in Section 3.2.1, let \mathcal{D} be subjected to both prescribed thermal (same as in the previous section) and elastic loads, such as displacement \mathbf{u}^{BC} and traction \mathbf{t}^{BC} . In addition to Eq. (11) (Wu, Zhang, Cui & Yin, 2023), thermoelastic boundary integral equations are introduced to handle temperature change as follows:

$$u_i^B(\mathbf{x}) = -\int_{\partial D^I} T_{ij}(\mathbf{x}, \mathbf{x}') u_j^{BC}(\mathbf{x}') d\mathbf{x}' + \int_{\partial D^u} G_{ij}(\mathbf{x}, \mathbf{x}') t_j^{BC}(\mathbf{x}') d\mathbf{x}'$$

$$-\int_{\partial D^T} K(\mathbf{x}') n_j(\mathbf{x}') G_{i,j'}(\mathbf{x}, \mathbf{x}') T^{BC}(\mathbf{x}') d\mathbf{x}' + \int_{\partial D^q} G_i(\mathbf{x}, \mathbf{x}') q^{BC}(\mathbf{x}') d\mathbf{x}'$$
(13)

where $T_{ij}(\mathbf{x}, \mathbf{x}')$ is fundamental solution of traction in *i*th direction caused by point force in *j*th direction, which can be expressed in terms of $G_{ij}(\mathbf{x}, \mathbf{x}')$,

$$T_{ij}(\mathbf{x}, \mathbf{x}') = \frac{C_{imkl}(\mathbf{x}')(G_{kj,l'} + G_{lj,k'})}{2} n_m(\mathbf{x}')$$
(14)

Subsequently, strain at a field point is obtained through partial derivatives as follows:

$$2\varepsilon_{im}^{BM}(\mathbf{x}) = -\int_{\partial D'} \left[T_{ij,m}(\mathbf{x}, \mathbf{x}') + T_{mj,i}(\mathbf{x}, \mathbf{x}') \right] u_j^{BC}(\mathbf{x}') d\mathbf{x}' + \int_{\partial D'} \left[G_{ij,m}(\mathbf{x}, \mathbf{x}') + G_{mj,i}(\mathbf{x}, \mathbf{x}') \right] t_j^{BC}(\mathbf{x}') d\mathbf{x}' - \int_{\partial D'} K(\mathbf{x}') n_j(\mathbf{x}') \left[G_{i,j'm}(\mathbf{x}, \mathbf{x}') + G_{m,j'i}(\mathbf{x}, \mathbf{x}') \right] T^{BC}(\mathbf{x}') d\mathbf{x}' + \int_{\partial D'} \left[G_{i,m}(\mathbf{x}, \mathbf{x}') + G_{m,i}(\mathbf{x}, \mathbf{x}') \right] q^{BC}(\mathbf{x}') d\mathbf{x}'$$
(15)

3.2.3. Global matrices of the boundary element method

As thermal and thermoelastic/elastic boundary integral equations provided by Eqs. (11) and (13), a global matrix involving both thermal and thermoelastic boundary integral equations can be constructed in the boundary element method (BEM). Let NN and dim denote the number of boundary nodes and the dimension of the problem; this scheme, specifically, involves a square dense global matrix with size $(\dim + 1)^2 \times NN^2$. When the number of DOFs increases, this scheme becomes expensive and inefficient, considering limited computational resources due to larger memory usage and more effort to solve a larger matrix. It is observed that thermal solutions are independent while thermoelastic/elastic solutions require coupling of thermal solutions. In this paper, we propose to separate the solving procedures for thermal and thermoelastic problems. The scheme with two global matrices only requires two matrices with size NN^2 and $\dim^2 \times NN^2$ for thermal and thermoelastic problems, respectively, while the same amount of calculation is needed for coefficients.

Through boundary discretization, boundary responses can be written as interpolations of nodal values. Subsequently, one can write the discretized boundary integral equations for thermal, thermoelastic problems, respectively.

$$T^{B}(\mathbf{x}) = \sum_{e=1}^{NE} \left[-HT^{e} + Uq^{e} \right], \quad u_{i}^{B}(\mathbf{x}) = \sum_{e=1}^{NE} \left[-H_{ij}u_{j}^{e} + U_{ij}t_{j}^{e} - H_{i}T^{e} + U_{i}q^{e} \right]$$

$$(16)$$

where H, H_i, H_{ij} and U, U_i, U_{ij} represents discretized boundary integral of G, G_i and G_{ij} , respectively; NE is the number of elements and the superscript e stands for quantities in the eth element.

$$H = \int_{S_e} K(\mathbf{x}') n_j(\mathbf{x}') G_{,j'}(\mathbf{x}, \mathbf{x}') N(\mathbf{x}') dS, \quad U = \int_{S_e} G(\mathbf{x}, \mathbf{x}') N(\mathbf{x}') dS$$

$$H_i = \int_{S_e} K(\mathbf{x}') n_j(\mathbf{x}') G_{m,j'}(\mathbf{x}, \mathbf{x}') N_{mi}(\mathbf{x}') dS, \quad U_i = \int_{S_e} G_m(\mathbf{x}, \mathbf{x}') N_{mi}(\mathbf{x}') dS$$

$$H_{ij} = \int_{S_e} T_{mi}(\mathbf{x}, \mathbf{x}') N_{mj}(\mathbf{x}') dS, \quad U_{ij} = \int_{S_e} U_{mi}(\mathbf{x}, \mathbf{x}') N_{mj}(\mathbf{x}') dS$$
(17)

Assembling coefficients of boundary integral equations in Eq. (17), the global matrix for thermal problem can be constructed as follows:

$$[H] [T^{BC}] = [U] [q^{BC}] \qquad \text{for the thermal problem}$$
 (18)

$$[H_{ij}] \left[u_j^{BC} \right] + [H_i] \left[T^{BC} \right] = \left[U_{ij} \right] \left[t_j^{BC} \right] + \left[U_i \right] \left[q^{BC} \right]$$
 for the thermoelastic problem (19)

The thermal boundary response can be obtained by solving the global equation system in Eq. (18), and then thermal effects are coupled through thermoelastic boundary integral equations in Eq. (19). Since BEM is a collocation method, strongly singular (r^{-2}) diagonal elements in [H], $[H_{ij}]$ can be handled through the method of rigid-body motion. Notice that only weak singularities r^{-1} exist in diagonal elements of $[H_i]$, which can be numerically evaluated by the conventional Gauss quadrature rule.

3.3. Dual equivalent inclusion method for bounded bimaterial domain

In Eshelby's celebrated works (Eshelby, 1957, 1959), when an ellipsoidal inhomogeneity is embedded in an infinite solid, it is proposed to simulate inhomogeneity with an inclusion with constant eigenstrain. The surrounding disturbed fields are obtained through volume integrals of fundamental solutions composed of biharmonic and harmonic potential functions, namely Eshelby's tensors. By fundamental solutions, the original EIM was further extended to heat conduction in full-space (Hatta & Taya, 1986) as well as bimaterial (Wang et al., 2022), where ETGs are introduced to handle mismatch of thermal conductivity. For the thermoelastic problems, the straight combination of thermal EIM and elastic EIM is trivial, where the main obstacle is the domain integral of varying temperature fields disturbed by ETGs. As mentioned in Section 3.1, fundamental solutions provide a response at the field point caused by excitation at the source point. Using Gauss' theorem, the full-space domain integrals of temperature can be mathematically transformed as domain integrals over the inhomogeneity, which introduces coupled thermal effects to elastic fields. A thermoelastic inclusion/inhomogeneity (DEIM) problem is first introduced, and DEIM is further combined with BEM for thermoelastic analysis in a bounded bimaterial domain.

3.3.1. Inclusions in two jointed dissimilar half spaces

Consider an infinite domain \mathcal{D} composed of two dissimilar half spaces embedded with multiple N_I subdomains Ω^I , exhibiting exactly the same material properties as \mathcal{D} . For an inclusion problem, Ω^I is subjected to prescribed eigen-fields, such as ETGs $T_i^{I*}(\mathbf{x}')$ and eigenstrains $\varepsilon_{ij}^{I*}(\mathbf{x}')$. Due to intensive interactions and disturbance by boundary, bimaterial interface and other subdomains elaborated in Section 3.3.2, the eigen-fields, including ETGs and eigenstrains, are provided in polynomial-form expanded at the center of Ω^I as Eq. (20),

$$T_{i}^{I*}(\mathbf{x}) = T_{i}^{I0*} + (x_{k} - x_{k}^{Ic})T_{ik}^{I1*} + (x_{k} - x_{k}^{Ic})(x_{l} - x_{l}^{Ic})T_{ikl}^{I2*} + \cdots$$

$$\varepsilon_{ii}^{I*}(\mathbf{x}) = \varepsilon_{ii}^{I0*} + (x_{p} - x_{p}^{Ic})\varepsilon_{iip}^{I1*} + (x_{p} - x_{p}^{Ic})(x_{q} - x_{q}^{Ic})\varepsilon_{iipq}^{I2*} + \cdots$$

$$(20)$$

where \mathbf{x}^{IC} is the center of subdomain Ω^I ; superscripts I0, I1, and I2 represent uniform, linear and quadratic polynomial terms, which are applied to approximate ETGs and eigenstrains in Ith subdomain. According to fundamental solution in Eq. (4), Eq. (5) and (9), the induced temperature (T) and displacement (\mathbf{u}) can be acquired,

$$T^{D}(\mathbf{x}) = \sum_{I=1}^{N_{I}} \int_{\Omega^{n}} K(\mathbf{x}') \frac{\partial G(\mathbf{x}, \mathbf{x}')}{\partial x'_{m}} T_{m}^{I*}(\mathbf{x}') dV(\mathbf{x}') = \sum_{I=1}^{N_{I}} D_{k}^{I} T_{k}^{I0*} + D_{kp}^{I} T_{kp}^{I1*} + D_{kpq}^{I} T_{kpq}^{I2*}$$

$$u_{i}^{D}(\mathbf{x}) = \sum_{I=1}^{N_{I}} \left[\int_{\Omega_{I}} \frac{\partial G_{ij}(\mathbf{x}, \mathbf{x}')}{\partial x'_{m}} \varepsilon_{kl}^{*}(\mathbf{x}') C_{jmkl}(\mathbf{x}') dV(\mathbf{x}') + \int_{\Omega_{I}} \frac{\partial G_{i}(\mathbf{x}, \mathbf{x}')}{\partial x'_{k}} T_{k}^{*}(\mathbf{x}') K(\mathbf{x}') dV(\mathbf{x}') \right]$$

$$= \sum_{I=1}^{N_{I}} g_{ikl}^{I} \varepsilon_{kl}^{I0*} + g_{iklp}^{I} \varepsilon_{kl}^{I1*} + g_{iklpq}^{I} \varepsilon_{klpq}^{I2*} + W_{ik}^{I} T_{kp}^{I0*} + W_{ikpq}^{I} T_{kpq}^{I1*} + W_{ikpq}^{I} T_{kpq}^{I2*}$$

$$(21)$$

where $D^I_{kpq...} = \int_{\Omega^I} G_{,k'}(x'_p - x^{IC}_p)(x'_q - x^{IC}_q)...dV(\mathbf{x}')$ is polynomial-form Eshelby's tensor relating ETGs to temperature; $g^I_{iklpq...} = \int_{\Omega^I} G_{ij,m'}C_{jmkl}(x_p - x^{IC}_p)(x_q - x^{IC}_q)...dV(\mathbf{x}')$ and $W^I_{ikpq...} = \int_{\Omega^I} G_{i,k'}K(x_p - x^{IC}_p)(x_q - x^{IC}_q)...dV(\mathbf{x}')$ are polynomial-form Eshelby's tensors relating eigenstrains and ETGs to displacement field, respectively. Subsequently, eigen-fields induced temperature gradients and

mechanical strain can be acquired through partial derivatives with Eq. (21).

$$T_{,i}^{D}(\mathbf{x}) = \sum_{I=1}^{N_{I}} D_{k,i}^{I} T_{k}^{I0*} + D_{kp,i}^{I} T_{kp}^{I1*} + D_{kpq,i}^{I} T_{kpq}^{I2*}$$

$$\varepsilon_{ij}^{DM}(\mathbf{x}) = \varepsilon_{ij}'(\mathbf{x}) - \alpha \Delta T(\mathbf{x}) \delta_{ij} = \sum_{I=1}^{N_{I}} \left\{ \left[S_{ijkl}^{I} \varepsilon_{kl}^{I0*} + S_{ijklp}^{I} \varepsilon_{klp}^{I1*} + S_{ijklpq}^{I} \varepsilon_{klpq}^{I2*} \right] + \left[R_{ijk}^{I} T_{k}^{I0*} + R_{ijkp}^{I} T_{kp}^{I1*} + R_{ijkpq}^{I} T_{kpq}^{I2*} - \alpha \delta_{ij} \left[D_{k}^{I} T_{k}^{I0*} + D_{kp}^{I} T_{kp}^{I1*} + D_{kpq}^{I} T_{kpq}^{I2*} \right] \right\}$$

$$(22)$$

where $S_{ijklpq}^{I} = \frac{g_{iklpq,j}^{I} + g_{jklpq,i}^{I}}{2}$ and $R_{ijkpq}^{I} = \frac{W_{ikpq,j}^{I} + W_{jkpq,i}^{I}}{2}$ are polynomial-form Eshelby's tensors relating eigenstrain, ETG to strain, respectively; α is the thermal expansion ratio. The analytical forms of the above domain integrals have been reported in our recent work (Wu, Zhang, & Yin, 2023). And the time consumption on calculating coefficients on inhomogeneities is elaborated in Section 3.3.4.

3.3.2. Inhomogeneities in bounded bimaterial domain

The previous subsection considers the inclusion problem in infinite bimaterial medium, where prescribed polynomial-form eigenfields exist over the subdomains. The application of a polynomial-form eigen-fields is necessary due to intensive interactions and other boundary effects, which is analogous to strain gradient theories (Ma et al., 2018). For practical applications, the assumption of an infinite medium is too ideal as experimental samples are bounded. In addition, shown as Fig. 2, the subdomain Ω^I generally exhibits different material properties, specifically stiffness, thermal modulus, and thermal conductivity. Since the boundary response is considered through BEM, the temperature and displacement can be obtained through superposition of Eqs. (11), (13) and (21).

$$T(\mathbf{x}) = T^{B}(\mathbf{x}) + T^{D}(\mathbf{x}) = \sum_{e=1}^{NE} \left[-HT^{e} + Uq^{e} \right] + \sum_{I=1}^{N_{I}} \left[D_{k}^{I} T_{k}^{I0*} + D_{kp}^{I} T_{kp}^{I1*} + D_{kpq}^{I} T_{kpq}^{I2*} \right]$$

$$u_{i}(\mathbf{x}) = u_{i}^{B}(\mathbf{x}) + u_{i}^{D}(\mathbf{x}) = \sum_{e=1}^{NE} \left[-H_{ij} u_{j}^{e} + U_{ij} t_{j}^{e} - H_{i} T^{e} + U_{i} q^{e} \right] + \sum_{I=1}^{N_{I}} \left\{ g_{ikl}^{I} \varepsilon_{kl}^{I0*} + g_{iklpa}^{I} \varepsilon_{kl}^{I1*} + g_{iklpa}^{I} \varepsilon_{klpa}^{I2*} + W_{ik}^{I} T_{kp}^{I0*} + W_{ikp}^{I} T_{kp}^{I1*} + W_{ikpa}^{I} T_{kpa}^{I2*} \right\}$$

$$(23)$$

where the temperature gradient and mechanical strain can be derived through a combination of Eqs. (12), (15) and (22). The polynomial-form ETGs can be determined through equivalent flux conditions as Eq. (24),

$$K^{w}(T_{i}^{B} + T_{i}^{D} - T_{i}^{I0*}) = K^{I}(T_{i}^{B} + T_{i}^{D})$$

$$K^{w}(T_{i,m}^{B} + T_{i,m}^{D} - T_{im}^{I1*}) = K^{I}(T_{i,m}^{B} + T_{i,m}^{D})$$

$$K^{w}(T_{i,m}^{B} + T_{i,mn}^{D} - 2T_{imn}^{I2*}) = K^{I}(T_{i,mn}^{B} + T_{i,mn}^{D})$$
(24)

where the superscript w is determined by the position of Ω^I that when $x_3' \ge 0$ w = ' and $x_3' < 0$ w = ''; T_i^B and T_i^D are temperature variation by thermal boundary response in Eq. (11) and eigen-fields in Eq. (21), respectively; $T_{i,m}$, $T_{i,mn}$ are first and second order partial derivatives of temperature. Following the same fashion, the polynomial-form eigenstrains can be determined through equivalent stress conditions as Eq. (25),

$$C_{ijkl}^{w}(\varepsilon_{kl}^{BM} + \varepsilon_{kl}^{I} + \varepsilon_{kl}^{E}) - A_{ij}^{H}\Delta T = C_{ijkl}^{I}(\varepsilon_{kl}^{BM} + \varepsilon_{kl}^{I}) - A_{ij}^{I}\Delta T$$

$$C_{ijkl}^{w}(\varepsilon_{kl,m}^{BM} + \varepsilon_{kl,m}^{I} - \varepsilon_{klm}^{I1*}) - A_{ij}^{W}\Delta T_{,m} = C_{ijkl}^{I}(\varepsilon_{kl}^{BM} + \varepsilon_{kl}^{I}) - A_{ij}^{I}\Delta T_{,m}$$

$$C_{ijkl}^{w}(\varepsilon_{kl,m}^{BM} + \varepsilon_{kl,m}^{I} - \varepsilon_{klm}^{I2*}) - A_{ij}^{W}\Delta T_{,mn} = C_{ijkl}^{I}(\varepsilon_{kl}^{BM} + \varepsilon_{kl}^{I}) - A_{ij}^{I}\Delta T_{,mn}$$

$$(25)$$

3.3.3. Global matrices of inclusion-based boundary element method

Using the volume integral on the equivalent inclusions or inhomogeneities and boundary integral on outer surface, one can obtain both temperature and displacement field. The DEIM provides eigen-fields on the inhomogeneities. Therefore, the global linear equation system can be set up as follows:

For thermal analysis only, thermal global matrix can be written as:

$$\begin{bmatrix} H & \dots & -D^{I0} & -D^{I1} & -D^{I2} & \dots \\ \vdots & \vdots & \vdots & \vdots & \vdots & \vdots \\ \Delta K^I H^{I1} & \dots & \Delta K^I D^{I0'} & \Delta K^I D^{I1'} & \Delta K^I D^{I2'} & \dots \\ \Delta K^I H^{I2} & \dots & \Delta K^I D^{I0''} & \Delta K^I D^{I1''} & \Delta K^I D^{I2''} & \dots \\ \Delta K^I H^{I3} & \dots & \Delta K^I D^{I0'''} & \Delta K^I D^{I1'''} & \Delta K^I D^{I2'''} & \dots \\ \vdots & \vdots & \vdots & \vdots & \vdots & \vdots \\ (NN+NI^T) \times (NN+NI^T) & \vdots & \vdots & \vdots \\ (NN+NI^T) \times (NN+NI^T) & (NN+NI^T) \times (NN+NI^T) \times (NN+NI^T) & (NN+NI^T) & (NN+NI^T) & (NN+NI^T) \times (NN+NI^T) & (N$$

The ranks of the matrix are marked under itself. $\Delta K^I = K^w - K^I$; NN is the number of boundary nodes; NI^T is the total number of ETGs, which is $3, 12, 30 \times N_I$ for uniform, linear, and quadratic terms, respectively. Superscripts I1-I3 of H, U represent the order of partial derivatives at the Ith inhomogeneity; superscripts I0-I2 of D stands for Eshelby's tensors for uniform, linear and quadratic

Table 1
Time consumption for the coefficient matrix on inhomogeneities.

Number of	Thermal (s)	Thermoelastic (s)	Total (s)
inhomogeneities			
$N_I = 1$	0.069	0.423	0.492
$N_I = 100$	0.089	0.991	1.08
$N_I = 500$	0.217	4.758	4.975
$N_I = 1,000$	0.473	12.642	13.115
$N_I = 2,000$	1.261	40.578	41.839
$N_I = 4,000$	5.047	153.811	158.858
$N_I = 6,000$	9.799	339.576	349.375
$N_I = 8,000$	18.252	591.002	609.254
$N_I=10,000$	28.109	938.853	966.962

Processor: Intel i9-13900K & RAM: DDR4 4400 MHz.

ETGs, respectively, which follows Eq. (24). As demonstrated in Section 3.2.3, to save computational resources, the thermal global matrix in Eq. (26) needs to be solved first, and corresponding ETGs and thermal boundary responses can be obtained.

When both temperature and thermal expansion are considered, the thermoelastic global matrix can be written as

$$\begin{bmatrix} H_{i} & \dots & -W^{I0} & -W^{I1} & -W^{I2} & \dots \\ \vdots & \vdots & \vdots & \vdots & \vdots & \vdots & \vdots \\ \Delta C^{I}H_{i}^{I1} - \Delta A^{I}H & \dots & \Delta C^{I}R^{I0} - \Delta A^{I}D^{I0} & \Delta C^{I}R^{I1} - \Delta A^{I}D^{I1} & \Delta C^{I}R^{I2} - \Delta A^{I}D^{I2} & \dots \\ \Delta C^{I}H_{i}^{I2} - \Delta A^{I}H^{I1} & \dots & \Delta C^{I}R^{I0'} - \Delta A^{I}D^{I0'} & \Delta C^{I}R^{I1'} - \Delta A^{I}D^{I1'} & \Delta C^{I}R^{I2'} - \Delta A^{I}D^{I2'} & \dots \\ \Delta C^{I}H_{i}^{I3} - \Delta A^{I}H^{I2} & \dots & \Delta C^{I}R^{I0''} - \Delta A^{I}D^{I0''} & \Delta C^{I}R^{I1''} - \Delta A^{I}D^{I1''} & \Delta C^{I}R^{I2''} - \Delta A^{I}D^{I2''} & \dots \\ \vdots & \vdots & \vdots & \vdots & \vdots & \vdots & \vdots \\ \Delta C^{I}H_{i}^{I1} & \dots & \Delta C^{I}S^{I0} & \Delta C^{I}S^{I1} & \Delta C^{I}S^{I2} & \dots \\ \Delta C^{I}H_{i}^{I1} & \dots & \Delta C^{I}S^{I0} & \Delta C^{I}S^{I1'} & \Delta C^{I}S^{I2'} & \dots \\ \Delta C^{I}H_{i}^{I1} & \dots & \Delta C^{I}S^{I0'} & \Delta C^{I}S^{I1'} & \Delta C^{I}S^{I2'} & \dots \\ \Delta C^{I}H_{i}^{I1} & \dots & \Delta C^{I}S^{I0'} & \Delta C^{I}S^{I1'} & \Delta C^{I}S^{I2'} & \dots \\ \Delta C^{I}H_{i}^{I1} & \dots & \Delta C^{I}S^{I0'} & \Delta C^{I}S^{I1'} & \Delta C^{I}S^{I2'} & \dots \\ \Delta C^{I}H_{i}^{I1} & \dots & \Delta C^{I}S^{I0'} & \Delta C^{I}S^{I1'} & \Delta C^{I}S^{I2'} & \dots \\ \vdots & \vdots & \vdots & \vdots & \vdots & \vdots & \vdots \\ -\Delta C^{I}U_{i}^{I1} & \Delta C^{I}U_{i}^{I2} & \Delta C^{I}U_{i}^{I1} & \Delta C^{I}U_{i}^{I2} & \Delta C^{I}U$$

where $\Delta C^I = C^w - C^I$ and $\Delta A^I = A^w - A^I$; NI^E is the total number of eigenstrains, which is $6,24,60 \times N_I$ for uniform, linear and quadratic terms, respectively. The definition of superscripts is the same as Eq. (26). Solving the global system of linear equations, one can obtain thermal/elastic boundary responses and eigen-fields. Subsequently, the thermoelastic fields can be determined using Eq. (23).

3.3.4. Time consumption for the coefficient matrix on inhomogeneities

This subsection aims to illustrate time consumption for the calculation of coefficients in Eqs. (21) and (22), which are eventually assembled in the global thermal/thermoelastic matrices. Table 1 shows the time consumption of such analytical domain integrals calculated by the Intel i9-13900K processor. Notice that although (Yin et al., 2022) has suggested setting the cut-off distance to improve computational efficiency due to the rapid vanishing properties of fundamental solution, the data in Table 1 considers interactions among all inhomogeneities without setting cut-off distances. Based on the above Table, the calculation of coefficients in the thermal matrix is much faster than that of the thermoelastic problem.

4. Numerical verification and computational comparison of iBEM

This section aims to illustrate the accuracy of the iBEM algorithm with FEM and further compare the computational costs in three aspects, (i) preprocess, such as domain/surface discretization; (ii) CPU and RAM usage; and (iii) computational time. In the following, the thermoelastic BEM is first verified through case studies of thermal and elastic fields, and subsequently the iBEM will be verified considering bimaterial interfacial effects along with intensive inhomogeneity interactions.

As a numerical verification, without the loss of any generality, the material properties are assigned as: (1) K' = 5 W/m K, $\mu' = 0.3$ MPa, $\nu' = 0.2$ and $\mathcal{A}' = 15$ kPa for the upper phase \mathcal{D}^+ ; (2) K'' = 10 W/m K, $\mu'' = 0.8$ MPa, $\nu'' = 0.25$ and $\mathcal{A}'' = 10$ kPa for the lower phase \mathcal{D}^- ; and (3) $K^I = 1$ W/m K, $\mu^I = 0.1$ MPa, $\nu^I = 0.1$ and $\mathcal{A}^I = 5$ kPa. As shown in Fig. 2, the dimensions $h_1 = h_2 = b = l = 1$ m are selected. The thermal and elastic boundary conditions are: (i) constant temperature 100 °C and uniformly

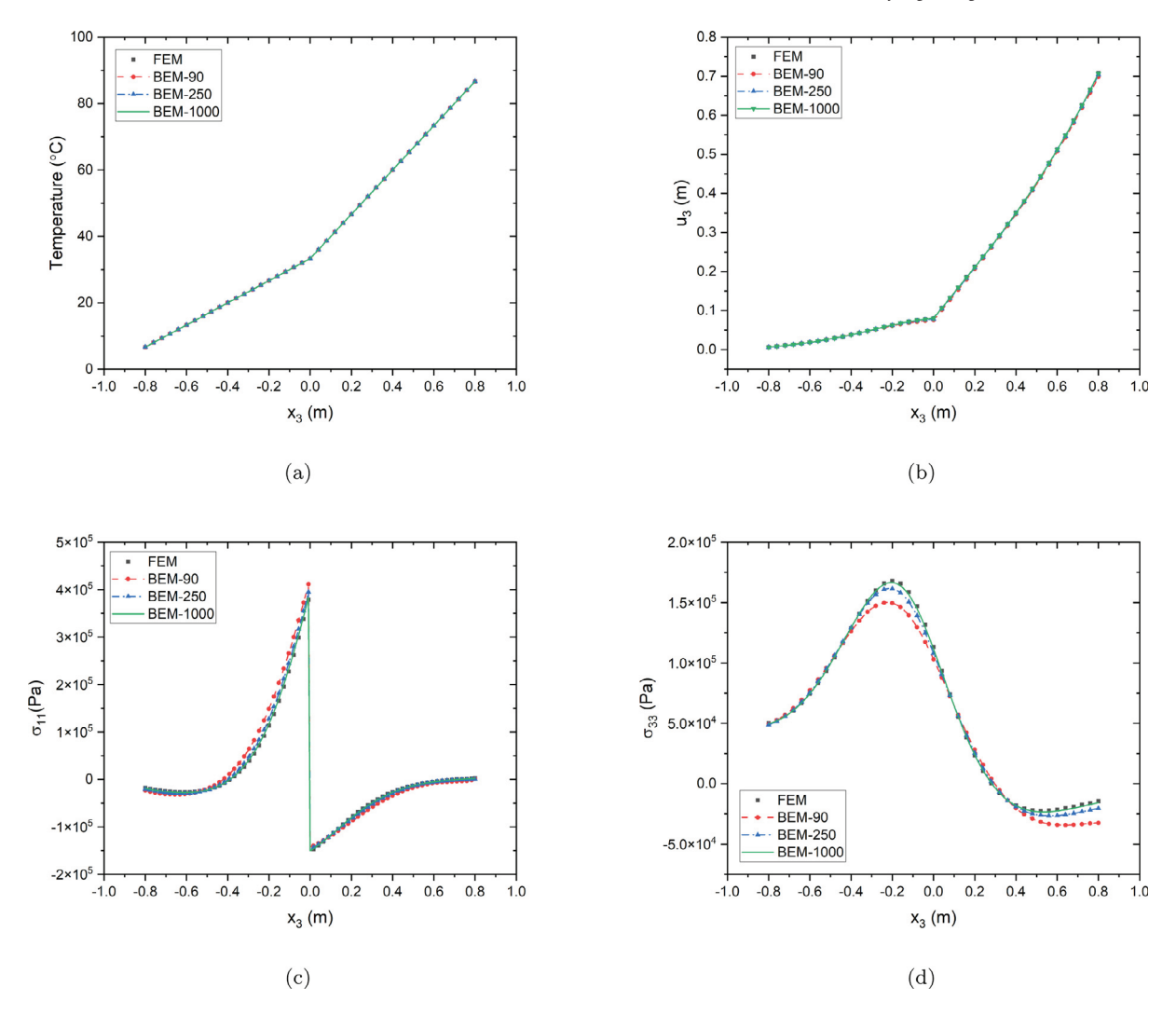


Fig. 3. Comparison and verification between the FEM with 250,000 hexagonal elements and the present BEM with 90,250,1000 quadrilateral elements of (a) temperature T, (b) vertical displacement u_3 , normal stresses (c) σ_{11} and (d) σ_{33} subjected to a linear temperature change and downward uniform load 10 kPa along the vertical symmetric line $x_3 \in [-0.8, 0.8]$ m.

applied downward pressure $10~\mathrm{kPa}$ on the top surface; (ii) constant temperature $0~\mathrm{^{\circ}C}$ and constrained displacement of the bottom surface; and (iii) all other four surfaces are insulated and traction-free. This section uses the commercial FEM software ANSYS to verify the variations of thermal and elastic fields.

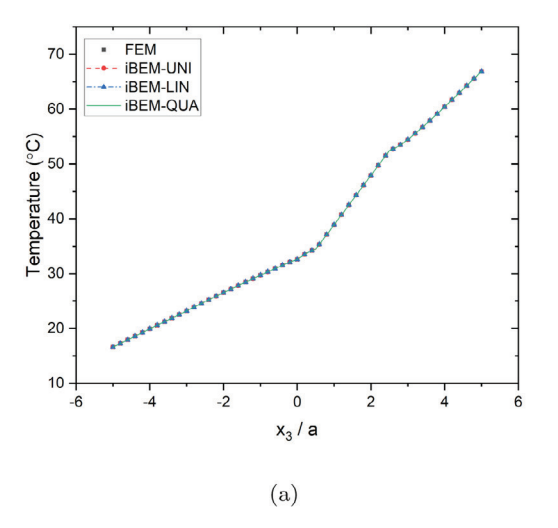
4.1. Comparison of thermoelastic fields between FEM and the single-domain BEM

To verify the convergence of the bimaterial BEM, results of 90,250, and 1000 boundary elements for the surface mesh are present below, where 4-node quadrilateral elements are used. As a well-established method, the convergence of the FEM results is not elaborated, but the final size step is provided. Since FEM applies domain integrals to couple thermal effects to elastic fields, it is important to adopt a similar (or the same) mesh to reduce numerical errors in thermal load (temperature) transfer between the "Steady-state thermal" and "Structural static" modules in ANSYS. Since the geometry is simple, a uniform global element size of 0.02 m is applied, and thus, the model adopts 250,000 hexagonal elements and 1,037,901 nodes.

Fig. 3 compares the temperature, displacement, and normal stresses between FEM and BEM with three surface meshes. Since the temperatures are prescribed on top and bottom surfaces, Fig. 3(a) exhibits a linear varying temperature. Due to the mismatch of thermal conductivity, the slope of the temperature suddenly changes at the bimaterial interface to satisfy the continuity of flux. As indicated, all curves agree well with each other on the description of temperature variation, which is important for thermoelastic modeling as the accuracy heavily relies on temperature change. Subsequently, Fig. 3(b) exhibits the variation of the displacement field. Although the curve "BEM-90" shows minor discrepancies when x_3 is close to 0.8 m, it agrees well with the other three cases.

Table 2
Comparison of the computational efficiency between FEM and BEM.

	CPU	RAM (Gb)	Mesh (s)	Data transfer (s)	Solving (s)
FEM-0.02-thermal	8	2.31	11.6	0	7.21
FEM-0.02-static	8	4.15	11.8	17.2	78.29
BEM-90	8	0.015	5	0	0.327
BEM-250	8	0.06	5	0	1.088
BEM-1000	8	0.77	5	0	7.912



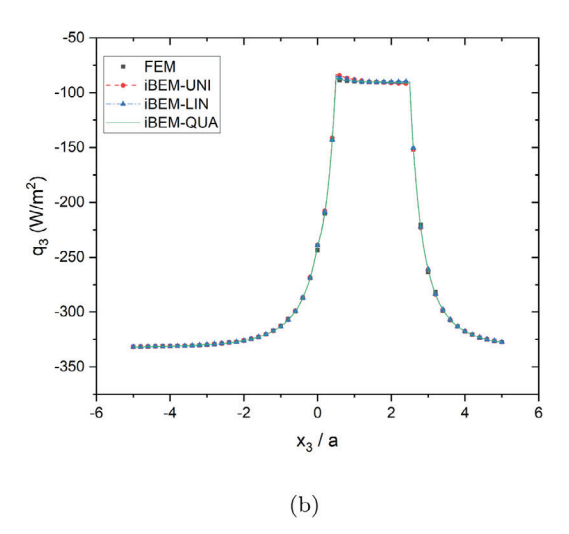


Fig. 4. Comparison and verification between FEM and dual iBEM with polynomial-form eigen-fields on (a) temperature T, (b) flux q_3 subjected to a linear temperature change along the vertical symmetric line $x_3/a \in [-5,5]$.

Figs. 3 (c) and 3 (d) compare normal stress σ_{11} and σ_{33} , and the main differences between FEM and BEM can be found with surface mesh 90 and 250 when x_3 is close to 0.8 m.

Before interpreting such a phenomenon, readers can first refer to Fig. 4 in Wu, Zhang, Cui and Yin (2023), which merely involves a comparison of elastic fields, and comparatively larger differences can be observed between the case of 90 elements and FEM. Due to the change in temperature and large thermal modulus, the thermal effects dominate, which changes the distribution of normal stresses. However, when comparing the results of three numbers of meshes, the difference between BEM and FEM becomes much smaller. This case study used 4 Gauss integral points and adopts an adaptive subdivision integration scheme. Therefore, the discrepancies with fewer elements should be interpreted as less accuracy in the description of boundary responses. Table 2 compares the time consumption and resource usage between the BEM and FEM methods.

4.2. Comparison of thermoelastic fields between FEM and iBEM with polynomial-form eigen-fields

In Eq. (20), the eigen-fields are expanded into a polynomial form at the center of each inhomogeneity to provide tailorable accuracy. The necessity of higher-order terms has been discussed extensively in the literature (Mura, 1987; Wu, Zhang, & Yin, 2023; Yin et al., 2022), especially when the local fields around the inhomogeneity are under intensive disturbance, such as close to the boundary, bimaterial interface or to other inhomogeneities. The distance ratio h/a has been used to measure interfacial and interaction effects, where a and h are the radius and distance from the inhomogeneity (Yin et al., 2022). Based on Eqs. (24) and (25), the polynomial-form eigen-fields can be determined, and they are found to be positively related to material mismatches, such as the difference between thermal conductivity and thermal modulus. Regarding the magnitude of disturbed fields caused by ETGs and eigenstrains, two primary factors determine their influences: their magnitude and distance between the field point and the inhomogeneity. Because the matrix and inhomogeneity exhibit greater material mismatch of thermal modulus, ETGs dominate local disturbed fields. Based on the definition of fundamental solutions, the disturbances by ETGs and eigenstrain on stress fields decay in r^{-1} and r^{-2} , respectively. Therefore, it is necessary to consider both ETGs and eigenstrains. For verification with FEM, 3,331,649 nodes and 2,453,741 10-node tetrahedral elements are used with distance ratio h/a = 1.2. Since only distance ratios change among cases, other cases h/a = 1.5, 2.0, 3.0 apply similar discretization.

4.2.1. One inhomogeneity subjected to interfacial effects

Fig. 4 compares the variation of temperature and flux q_3 among FEM and iBEM with three orders of polynomial-form ETGs when the distance ratio h/a = 1.5. The differences among the four curves can barely be identified for the thermal fields, particularly for temperature. Slight discrepancies of the curve "iBEM-UNI" of flux are observed at the entering point of the inhomogeneity on

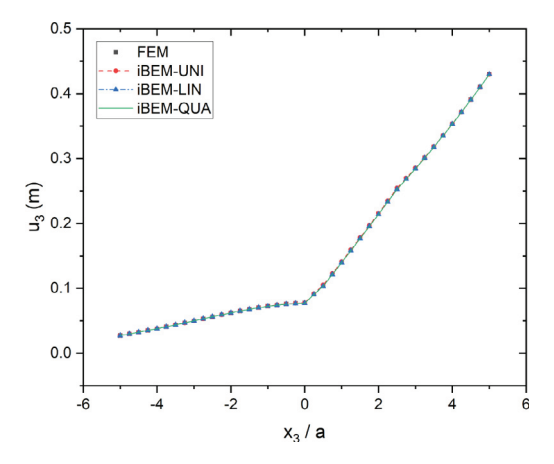


Fig. 5. Comparison and verification between FEM and dual iBEM with polynomial-form eigen-fields on displacement component u_3 subjected to a linear temperature change and a uniform downward pressure 10 kPa along the vertical symmetric line $x_3/a \in [-5, 5]$.

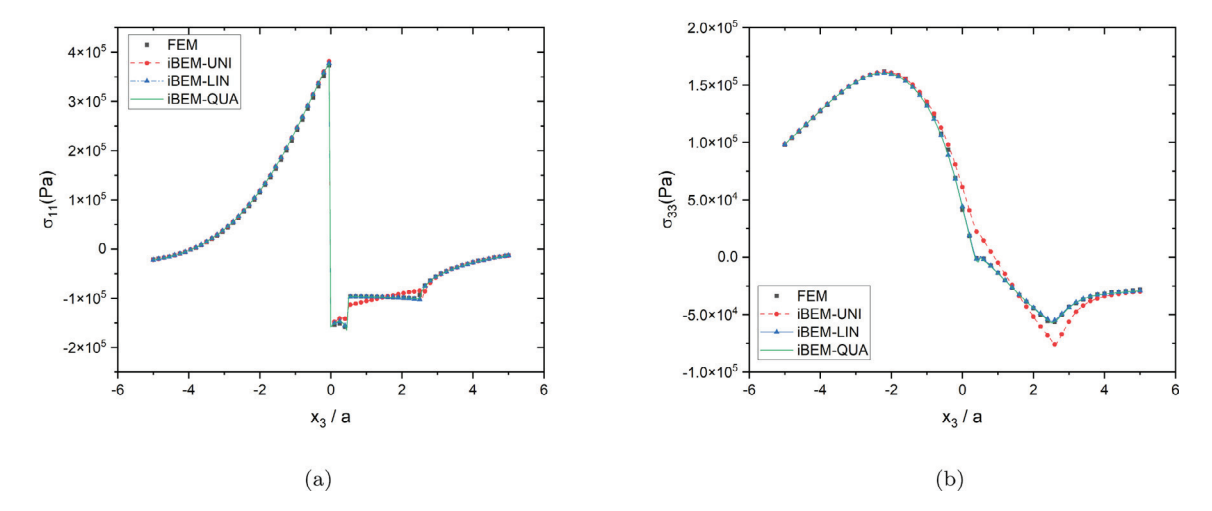
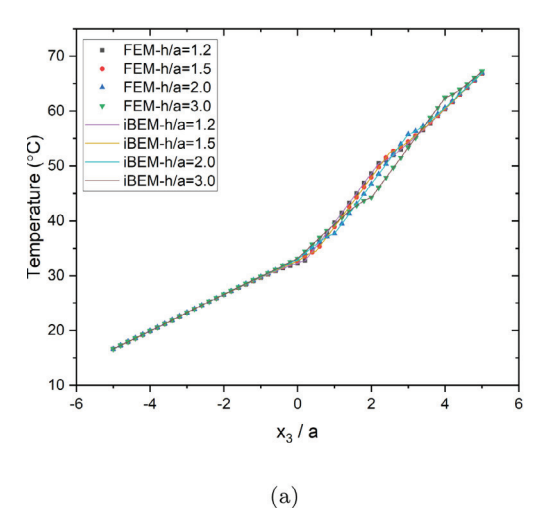


Fig. 6. Comparison and verification between FEM and dual iBEM with polynomial-form eigen-fields on normal stresses (a) σ_{11} and (b) σ_{33} subjected to a linear temperature change and a uniform downward pressure 10 kPa along the vertical symmetric line $x_3/a \in [-5, 5]$.

Fig. 4(b) since the uniform ETG may not be adequate to describe thermal disturbance by the bimaterial interface. Therefore, even uniform eigen-fields can provide good prediction at most field points. Notice that the accuracy of thermal fields significantly impacts the stress field prediction. The reasons are that (i) temperatures directly associated with thermal modulus and (ii) flux are indeed partial derivatives of temperature, which affects the subsequent solutions with higher-order eigenstrains.

Fig. 5 shows the displacement field caused by a linear temperature change and a pressure. Although the "iBEM-UNI" may not provide the most accurate prediction, the four curves on displacement u_3 agree well with each other. Subsequently, Figs. 6(a) and 6(b) support our preceding conclusion on negative effects caused by an inaccurate thermal field. It is observed that in both figures of normal stresses, the "iBEM-UNI" curve exhibits obvious discrepancies among FEM and iBEM with linear and quadratic terms. Such large numerical error can be interpreted as an accumulation of thermal predictions and the rough assumption of the uniform eigenstrain distribution. As illustrated in Figs. 3(c) and 3(d), the initial fields without the inhomogeneity are non-uniform (approximately linear around the position of inhomogeneity). Therefore, the assumption of merely uniform eigenstrains is not accurate enough, and the higher-order variations should be considered. In Figs. 6(c) and 6(d), the results of "iBEM-LIN" and "iBEM-QUA" are close. Such phenomenon can be interpreted as a consequence of linear varying temperature fields and thus similar stress fields.

Verifying uniform, linear, and quadratic order eigen-fields indicates that higher-order terms can better describe local fields. Hence, Figs. 7–9 only use quadratic terms. This subsection aims to investigate the bimaterial interfacial effects by adjusting distance ratios h/a = 1.2, 1.5, 2.0, and 3.0, respectively. Similar to a case study of h/a = 1.5, the comparison of higher-order fields, i.e., displacement and temperature, exhibits better agreement than stress and flux. With quadratic terms, the discrepancies can seldom be noticed between the iBEM and FEM in Figs. 7 (a) and 8.



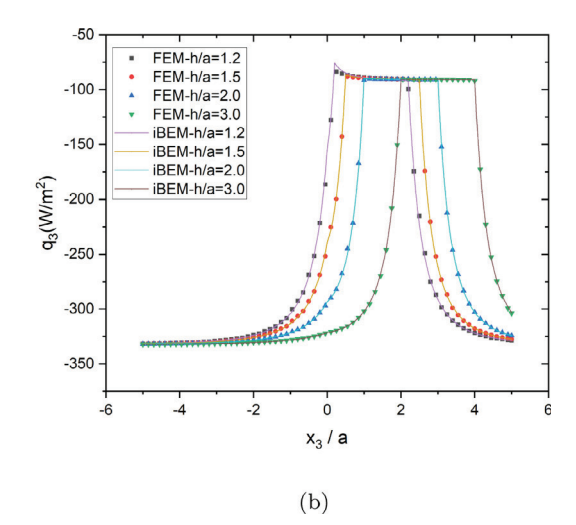


Fig. 7. Comparison and verification between FEM and dual iBEM with quadratic eigen-fields on (a) temperature T, (b) flux q_3 subjected to a linear temperature change along the vertical symmetric line $x_3/a \in [-5, 5]$ when distance ratios h/a = 1.2, 1.5, 2.0 and 3.0.

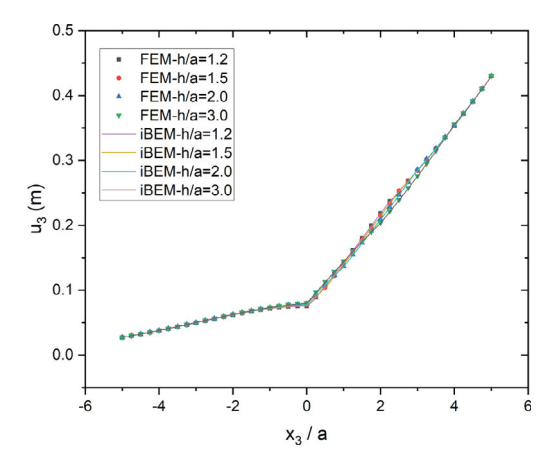


Fig. 8. Comparison and verification between FEM and dual iBEM with polynomial-form eigen-fields on displacement component u_3 subjected to a linear temperature change and a uniform downward pressure 10 kPa along the vertical symmetric line $x_3/a \in [-5,5]$ when distance ratios h/a = 1.2, 1.5, 2.0 and 3.0.

In addition, the interfacial effects disturb local thermal fields, resulting in a larger variation of temperature and higher flux in the neighborhood of the bottom region of the inhomogeneity. As discussed above, such interfacial effects on thermal fields accumulate, significantly influencing the corresponding stress. Fig. 9(a) presents the variation of normal stress σ_{11} , and it is observed that the jump of the normal stresses drastically increases with less distance ratios. For instance, the difference at the bottom of inhomogeneity (h/a = 1.2) is approximately 6 times compared with that of h/a = 3. Such interfacial effects can be considered a constraint since the lower phase D^+ is filled with stiffer material. Moreover, a similar trend can also be observed in Fig. 9(b).

Table 3 compares the usage of computational resources between the FEM and iBEM on the case study with distance ratio h/a = 1.2. Since FEM couples the thermal effects through volume integrals, as shown, "FEM-static" consumes a much longer time than that in Table 2 to obtain convergent thermal effects, which is generally computationally expensive. Among iBEM with three orders of eigen-fields, the linear and quadratic terms are capable of reproducing high-fidelity results as FEM. The iBEM is much faster since it analytically limits source domain integrals within the inhomogeneity.

4.2.2. Two top-down and side-by-side inhomogeneity interactions

The previous case studies investigated the performance of the iBEM considering bimaterial interfacial effects through adjusting distance ratios, which draws preliminary conclusions on the necessity to employ polynomial-form eigen-fields. Following the same fashion, this subsection aims to provide more insights into inhomogeneity interactions. The material properties, dimensions, and boundary conditions remain the same. In the following, two alignments of inhomogeneities are studied, (i) the top-down case that two inhomogeneities are placed in two phases along the vertical center line with distance h = 0.2a to the bimaterial interface; (ii) the side-by-side case that two inhomogeneities are placed in the upper phase \mathcal{D}^+ (h = 1.5) with horizontal distance 0.5a.

Table 3 Comparison of efficiency among iBEM and FEM on case of h/a = 1.2.

	CPU	RAM (Gb)	Mesh (s)	Data transfer (s)	Solving (s)
FEM-thermal	8	4.52	24.46	0	35.45
FEM-static	8	14.08	24.46	46.59	324.04
iBEM-UNI	8	0.77	5	0	8.35
iBEM-LIN	8	0.79	5	0	8.90
iBEM-QUA	8	0.81	5	0	15.426

Table 4
Comparison of efficiency among iBEM and FEM on case of top-down inhomogeneity interactions.

	CPU	RAM (Gb)	Mesh (s)	Data transfer (s)	Solving (s)
FEM-thermal	8	13.89	15.6	0	166.59
FEM-static	8	5.50	15.6	30.08	99.04
iBEM-UNI	8	0.78	5	0	8.318
iBEM-LIN	8	0.80	5	0	8.949
iBEM-QUA	8	0.82	5	0	21.104

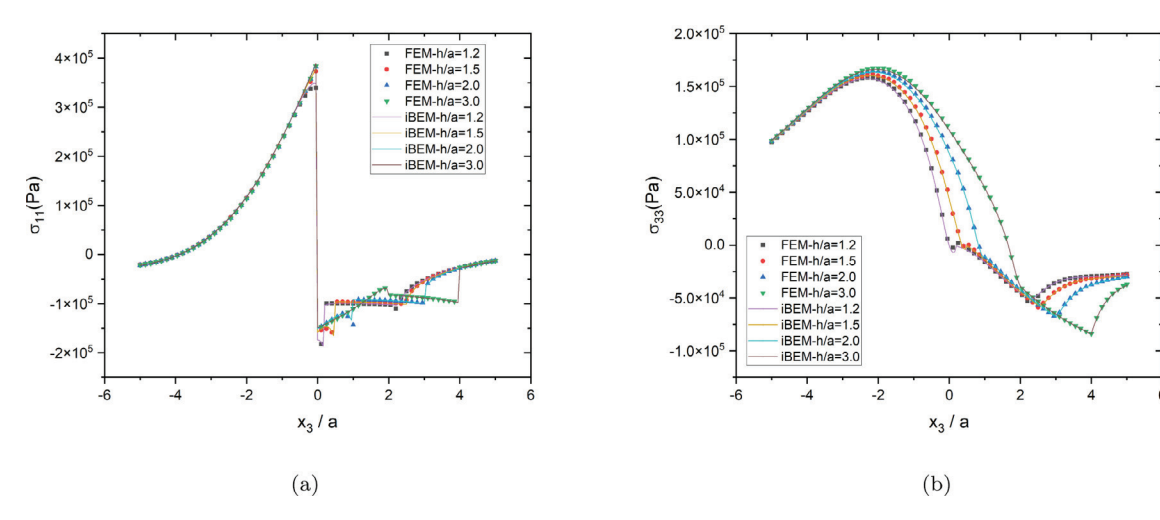


Fig. 9. Comparison and verification between FEM and dual iBEM with polynomial-form eigen-fields on normal stresses (a) σ_{11} and (b) σ_{33} subjected to a linear temperature change and a uniform downward pressure 10 kPa along the vertical symmetric line $x_3/a \in [-5,5]$ when distance ratios h/a = 1.2, 1.5, 2.0 and 3.0.

In general, the comparison of temperatures shows minor discrepancies. As indicated in Fig. 10(c), the curve of uniform eigenfields tends to have a wrong trend when x_1 is close to zero. However, the numerical errors regarding temperature are only 0.02%. As for flux q_3 , Fig. 10(b) exhibits relatively large differences around the bimaterial interface. Although the quadratic eigen-fields can accurately describe most interior parts of flux fields, FEM results indicate a more flattened trend. Notice that the two inhomogeneities are subjected to intensive interfacial effects and interactions. Consequently, it causes more complex fields, which require even higher order source fields to describe the sudden variations, and therefore, the quadratic terms may not be adequate. Since the influence of source fields is related to distance, a larger distance between inhomogeneities is accompanied by less intensive interactions, which is supported by Fig. 10(d) with distance from 0.4a to 0.5a.

Figs. 11(a) and (d) show that the variation of displacements and iBEM with three orders of eigen-fields agree well with the results of FEM. As interpreted in Section 4.2.2, the initial thermal field is approximately linear, and a linear temperature variation will result in linear non-mechanical strains. Therefore, the assumption of a uniform eigenstrain is not appropriate. Figs. 11(b-c) and Figs. 11(e-f) have demonstrated the limitation of using merely uniform terms. However, the main differences between uniform and other higher-order terms exist within inhomogeneities and have limited impact on further exterior field points. Table 4 compares the computational resource usage between iBEM and FEM, and 1,062,729 nodes and 785,124 elements are used in FEM.

5. Applications to a ceramic-metal FGM composite - Ni/Al₂O₃

The ceramic–metal FGM composite has been widely applied to avoid singularity issues associated with bimaterial interfacial effects, which aims to reduce intensive thermal stresses and takes advantage of the thermal resistance of ceramic. As one typical example, Ni/Al₂O₃ FGM composite can be described by three phases, namely (i) Nickel (height h_n), (ii) gradation (height h_g) and (iii) Al₂O₃ (height h_a), where the phase gradation only exist in (ii). Suresh and Mortensen (1997) summarized thermomechanical behaviors of FGMs and defined the gradation ratio, i.e., $h_g/(h_n + h_g + h_a)$ in this manuscript. According to their review, more minor

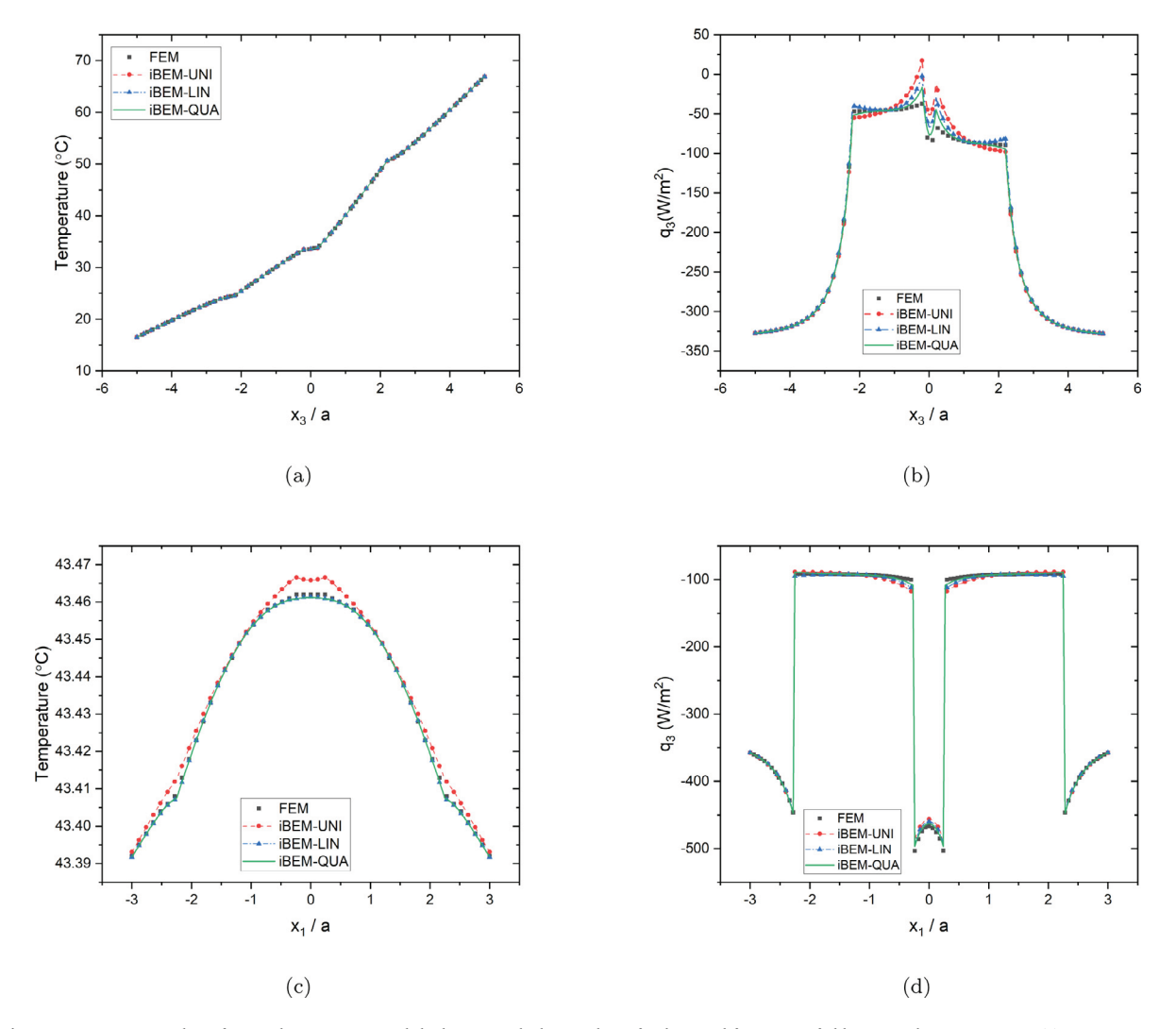


Fig. 10. Comparison and verification between FEM and dual iBEM with three orders of polynomial-form eigen-fields on top-down interaction (a) temperature T, (b) flux q_3 along the vertical center line $x_3/a \in [-5,5]$; and side-by-side interaction (c) temperature T, (d) flux q_3 along the horizontal center line $x_1/a \in [-3,3]$.

thermal stresses are expected with larger gradation ratios, which can be straightforwardly interpreted as effects of the microstructure and volume fraction.

5.1. Uniform temperature change

Since this section aims to illustrate iBEM on handling FGM composite, the effect of gradation ratios on averaged thermal stress fields is investigated. To control disturbances resulting from different inhomogeneity distributions and subsequent thermal effects, as indicated in Fig. 12(a-b), inhomogeneities are uniformly distributed within the gradation region. The gradation region is evenly divided into num layers, and the volume fraction of each layer follows the linear gradation in x_3 direction. Therefore, inhomogeneities are located at the same position for each layer but with increasing radius to achieve a specific volume fraction. For example, Fig. 12(a) plots 7776 inhomogeneities with num = 24 divisions, when $h_n = h_a = 1.67 \times 10^{-3}$ m and $h_g = 4h_a$. When the gradation ratio changes, it significantly impacts thermal fields. Hence, to avoid such disturbance, this section only considers uniform temperature increase of 100 °C, and the effects of such thermal effects will be studied in the following section.

According to Suresh and Mortensen (1997), the thermomechanical properties of nickel and aluminum oxide are (i) $\mu^n = 76.73$ GPa, $\nu^n = 0.3$, $K^n = 90.7$ W/K m², $A^n = 7.681$ MPa; and (ii) $\mu^a = 157.2$ GPa, $\nu^a = 0.25$, $K^a = 30.1$ W/K m², $A^a = 5.816$ MPa. The elastic boundary conditions are (i) the vertical displacement component is constrained of the bottom surface $x_3 = -0.005$ m, and (ii) all other surfaces are free of traction. Five gradation ratios, ratio = 1,5/6,2/3,1/2, and 2/5, are selected, and their resultant averaged thermal stresses are compared with the bimaterial case (without gradation). Figs. 13(a-d) plot variation of averaged thermal stresses along x_3 . To acquire the averaged stress fields, for instance, (i) the FGM sample indicated in Fig. 12 is first evenly divided

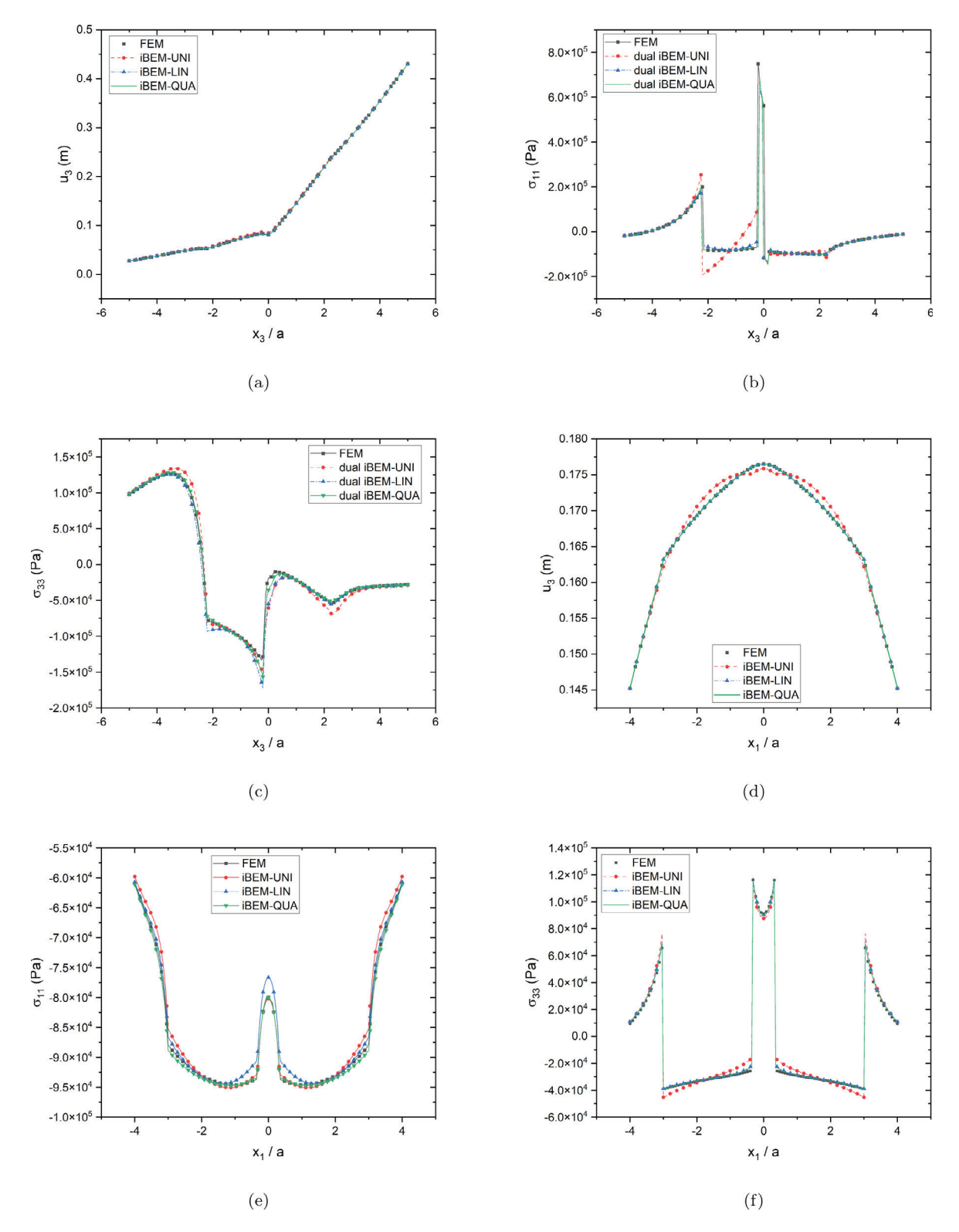


Fig. 11. Comparison and verification between FEM and dual iBEM with three orders of polynomial-form eigen-fields on top-down interaction (a) displacement u_3 , (b) σ_{11} , (c) σ_{33} along the vertical center line $x_3/a \in [-5,5]$; and side-by-side interaction (d) displacement u_3 , (e) σ_{11} , (f) σ_{33} along the horizontal center line $x_1/a \in [-3,3]$.

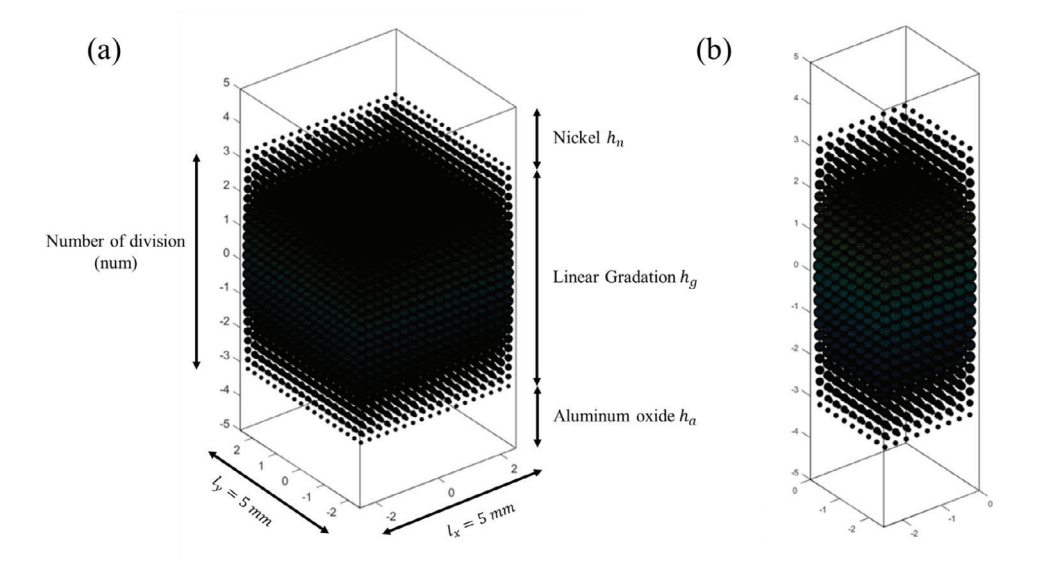


Fig. 12. Schematic plot of a FGM composite with dimension l_x, l_y and h_n, h_g, h_a embedded with uniformly distributed spherical inhomogeneities subjected to uniform temperature increase 100°C, (a) the sample $(x_1, x_2 \in [-0.0025, 0.0025] \text{ m}, x_3 \in [-0.005, 0.005] \text{ m})$ and (b) one quarter of the sample $(x_1, x_2 \in [-0.0025, 0.0025] \text{ m})$, $x_3 \in [-0.005, 0.005] \text{ m})$.

into num = 24 layers along the height direction (x_3) ; (ii) for each layer, its length $(x_1$ direction), width $(x_2$ direction) and height (x_3) direction are evenly divided into 10,10 and 20 for the quarter of the sample, which generates $10 \times 10 \times 20$ small cuboids; (iii) sampling points are located at the center of each small cuboids, and thus 2000 uniformly distributed sampling points in each layer and totally 48,000 sampling points for the quarter of the sample. In such a case, the averaged stress in Figs. 13 (a-d) is a volume-averaged quantity, which are not calculated based on the cross-section.

Indicated in Fig. 13(a), when there exists no gradation region, normal stress σ_{11} increases significantly in the neighborhood of the bimaterial interface due to material mismatch. Walpole (1996) has demonstrated such a phenomenon, where singular stress issues are expected. The intensive bimaterial effect and its significant stress can lead to the failure of the structure, such as delamination. When the gradation ratio is 2/5, the definition of the previously mentioned bimaterial interface becomes vogue since the materials cross $x_3 = 0$ exhibit continuous change, which improves stress singularity issues. As the gradation ratio increases, the magnitude of the maximum σ_{11} rapidly decreases. For the case "ratio = 1", the maximum σ_{11} around $x_3 = 0$ reduces to 14.43 MPa, while other cases are 19.38, 22.74, 46.2, and 105.52 MPa for gradation ratio equals 5/6, 2/3, 1/2 and 2/5, respectively. In addition, the variation trend of thermal stress σ_{11} differs from the bimaterial case.

Figs. 13(b) and (c) shows the variation of averaged thermal shear stress τ_{12} and τ_{13} along x_3 direction. Similar to the case of σ_{11} , the variation trend of shear stress becomes different due to the gradually changing microstructure, and the maximum shear stress reduces with the increase of gradation ratio. Oppositely, as indicated in Fig. 13(c), the maximum shear stress τ_{13} increases with the gradation ratio. It is observed in Fig. 13(d) the averaged thermal stress σ_{33} of cases "ratio = 1, 5/6, 2/3" exhibit smaller maximum σ_{33} than the bimaterial one. Then it increases significantly with the case "ratio = 2/5". Moreover, although the gradation region reduced σ_{11} , it also causes increase of σ_{33} . See $x_3 \in [-0.005, -0.002]$ m in Fig. 13(d).

Figs. 14(a-b), Figs. 15(a-b) and Figs. 16(a-b) plot the normal thermal stress contour of one-quarter structure (as shown in Fig. 12(b)), respectively. Comparing the stress contours, although the stress distribution within the gradation region is similar, the maximum magnitude of normal stresses changes from 805,915 to 1990, which indicates the same trend of the averaged fields. When the FGM range is smaller, the stress variation range is larger.

5.2. Effects of size and distribution of inhomogeneities

The preceding section presents an FGM composite subjected to uniform temperature increase with five gradation ratios and illustrates how iBEM handles the microstructure variation of linearly distributed inhomogeneities. In general applications, it is more likely that the FGM composite experienced more complex thermal conditions, such as the combination of prescribed temperature and flux. To illustrate iBEM's capability to handle the above scenarios, the thermal boundary conditions are revised as (i) zero reference temperature on the bottom surface, (ii) $100~\mathrm{W/m^2}$ heat flux on the top surface, and (iii) all other surfaces are insulated. The elastic boundary conditions are retained as in the previous section, and the gradation ratio is 1.

This section considers four numbers of divisions, num = 20, 24, 32 and 48, which leads to 2000, 3456, 7776 and 27,648 inhomogeneities (500, 864, 1944 and 6912 of the quarter structure). Notice that although inhomogeneities are linearly distributed along x_3 direction, the volume fraction of inhomogeneities decreases with the increase of height division (num). Taking the half structure

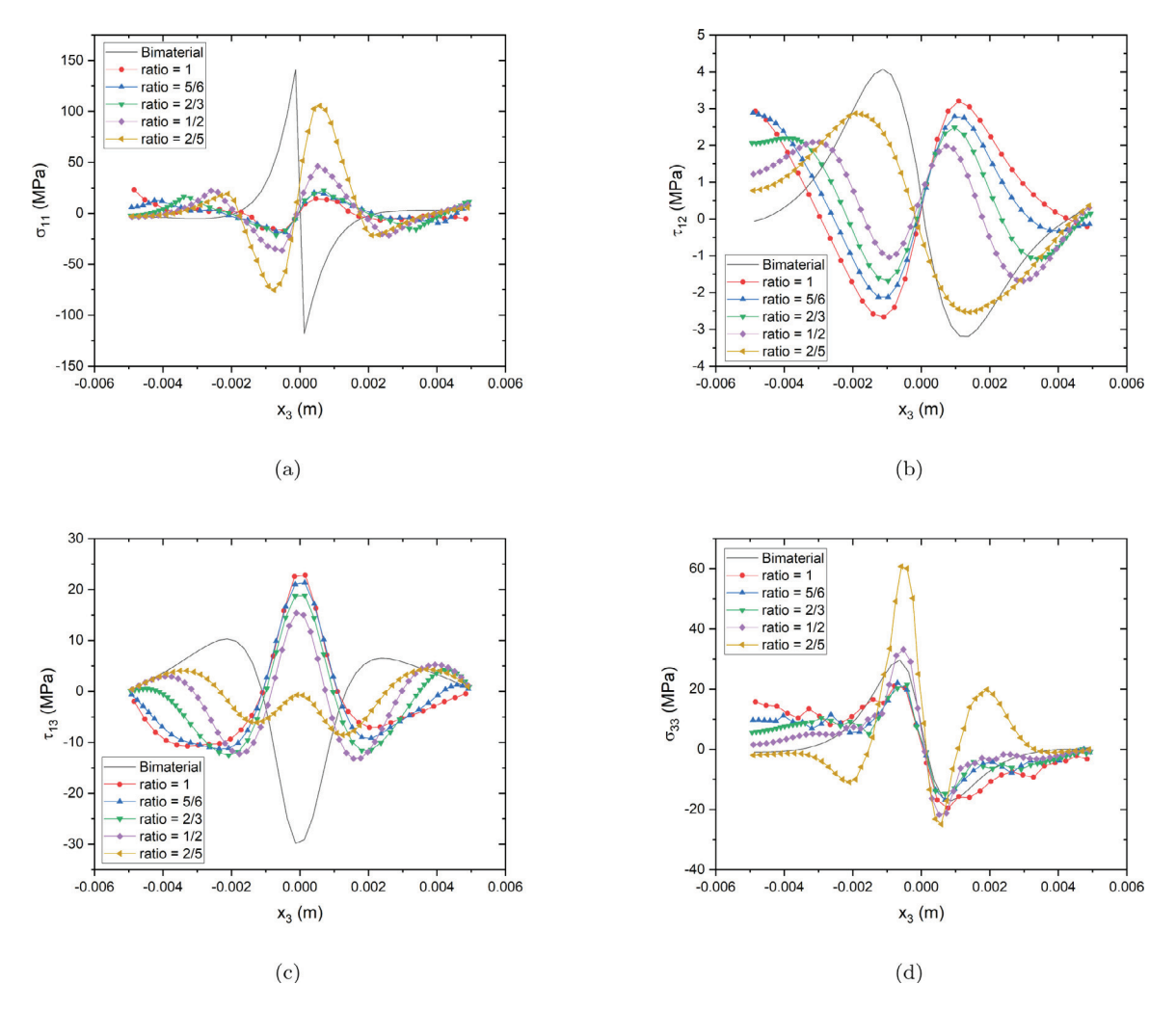


Fig. 13. Comparison and variations of spatial-averaged thermal stresses along the gradation direction, (a) σ_{11} , (b) τ_{12} , (c) τ_{13} and (d) σ_{33} versus different gradation ratios 1,5/6,2/3,1/2 and 2/5 subjected to uniform 100 temperature increase from a stress-free state.

(the upper phase) as an instance, the volume fractions are 0.325, 0.313, 0.297, and 0.281, and when $num \to \infty$, the volume fraction of the linear gradation is 0.25. Fig. 17(a) plots the variation of averaged temperature along the gradation direction. Interestingly, although the volume fractions, size, and distribution differ, the averaged temperature for the four curves is the same. The other four curves are smooth compared to the bimaterial case, which exhibits a sudden slope change. This can be interpreted as no obvious material mismatch crossing the former bimaterial interface. Fig. 17(b) and Fig. 17(e) plot the variation of averaged σ_{11} and σ_{33} , respectively. Similar to case studies as Fig. 13(a-d), the gradation region significantly reduces the maximum normal stresses. When num increases, the maximum stress reduction is less, which can be interpreted as a smaller volume fraction. Fig. 17(c) and Fig. 17(d) indicates the variation of averaged shear stress τ_{12} and τ_{13} , respectively. Similarly, the reduction of maximum stress increases with the decrease of num.

As Fig. 17 demonstrates the variation of the averaged thermomechanical behavior of the FGM composites, the stress variation along inhomogeneity interfaces, such as σ_{rr} and $\sigma_{\theta\theta}$, generally exhibit stress concentration effects, which may lead to local failure of the FGM composites. Therefore, it is important to investigate and evaluate some examples of such stress concentration. As reported in Wu, Zhang, and Yin (2023), the intensive interaction among inhomogeneities and bimaterial interface can cause strong stress concentration effects and angle shift of the maximum stress.

In the following, this subsection considers two adjacent layers of inhomogeneities close to the bimaterial interface of the quarter structure. Shown as Fig. 18, the number of inhomogeneities in each layer changes accordingly when the number of height divisions changes. Specifically, num = 20, 24, 32, 48 and the corresponding n = 25, 36, 64, 144, respectively. For simplicity, 4 pairs of inhomogeneities, highlighted by the blue rectangle, are selected to plot stress variation along two circumferences. The primary reason for such selection is that those inhomogeneities are subjected to intensive interfacial effects, boundary effects, and interactions among other inhomogeneities. For each inhomogeneity, two circumferences, the vertical (x_1-x_3) and horizontal (x_1-x_2) ones, where

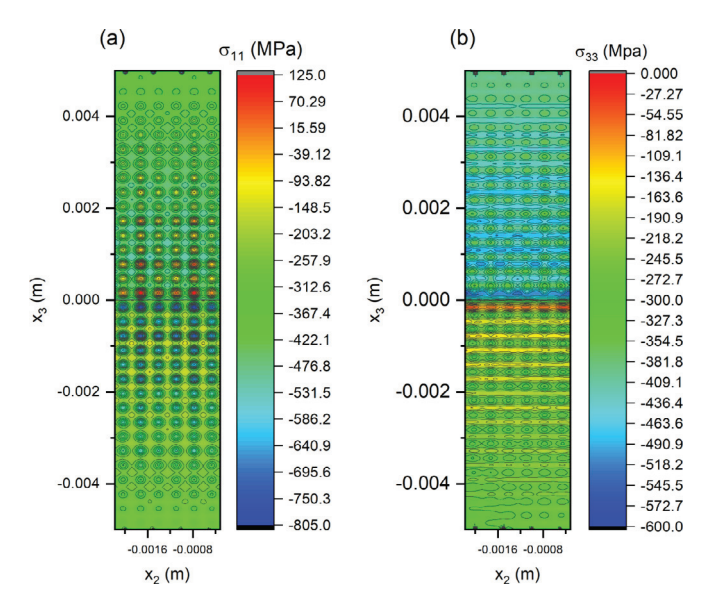


Fig. 14. Thermal stress contour of the internal cross-section of one quarter structure ($x_2 \in [-0.00218, -0.00032]$ m, $x_3 \in [-0.00499, 0.00499]$ m) with gradation ratio 1 subjected to uniform 100 °C temperature increase from a stress-free state.

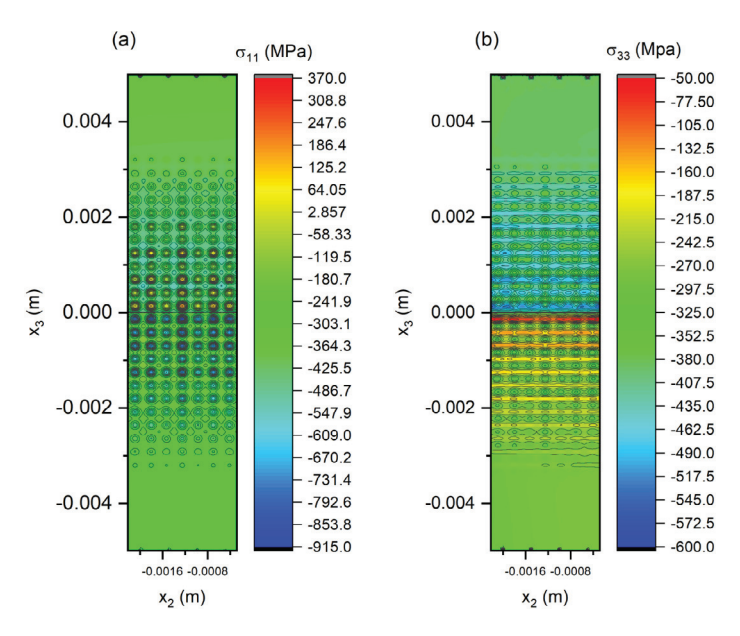


Fig. 15. Thermal stress contour of the internal cross-section of one quarter structure $(x_2 \in [-0.002215, -0.000285] \text{ m}, x_3 \in [-0.00499, 0.00499] \text{ m})$ with gradation ratio 2/3 subjected to uniform 100 °C temperature increase from a stress-free state.

40 uniformly distributed observing points are located. When the angle θ starts from x_1 axis, $\theta = 0, \frac{\pi}{40}, \frac{\pi}{20}, \dots, \frac{39\pi}{20}$ are considered. Since the FGM composites are only subjected to external thermal load (without external mechanical load), to reveal the phenomenon of stress concentration, two normal components σ_{rr} and $\sigma_{\theta\theta}$ are normalized by averaged stress components. The calculation of averaged normal and tangential stresses are obtained through Eq. (28),

$$\sigma_{rr}^{H/V} \text{ or } \sigma_{\theta\theta}^{H/V} = \sum_{i=1}^{n \times 40} \frac{|\sigma_{rr}^{i}| \text{ or } |\sigma_{\theta\theta}^{i}|}{n \times 40}, \quad n = 25, 36, 64, 144$$
 (28)

where H and V represent quantities calculated in horizontal or vertical circumference, respectively. Based on the calculation, the averaged stress are provided in Table 5,

For more details, plots of stress concentration for two cases num = 24 and num = 32 are elaborated in the Supplemental Information. As demonstrated, the selected four pairs of inhomogeneities are subjected to intensive bimaterial interfacial effects

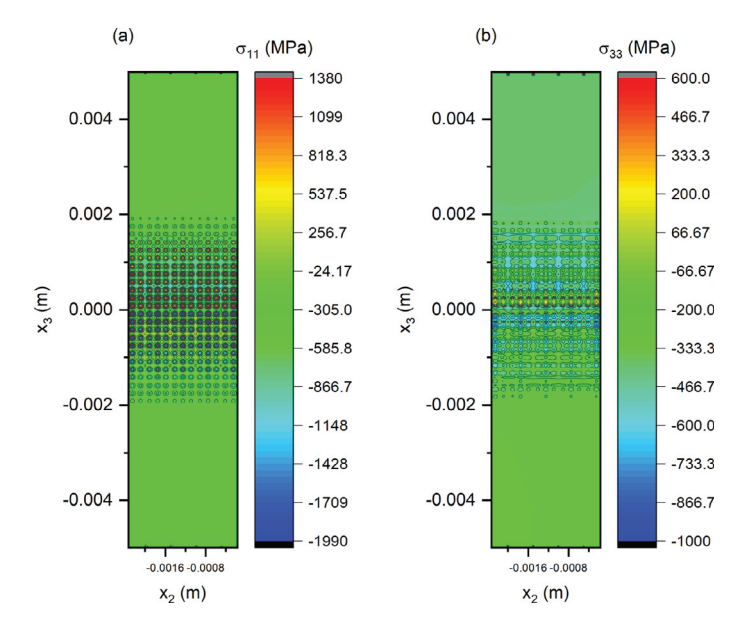


Fig. 16. Thermal stress contour of the internal cross-section of one quarter structure $(x_2 \in [-0.00233, -0.000171] \text{ m}, x_3 \in [-0.00499, 0.00499] \text{ m})$ with gradation ratio 1/2 subjected to uniform 100 °C temperature increase from a stress-free state.

Table 5

Averaged stress of adjacent layers of the bimaterial interface

n	Position of the layer	σ_{rr}^{V} (MPa)	$\sigma^V_{ heta heta}$ (MPa)	σ_{rr}^{H} (MPa)	$\sigma_{\theta\theta}^H$ (MPa)
25	up	0.016946	0.0217784	0.0194782	0.0212711
25	down	0.0205907	0.0300842	0.0227368	0.0274418
36	up	0.0214511	0.024721	0.0214511	0.024721
36	down	0.0205734	0.0155885	0.0205734	0.0155885
64	up	0.027866	0.0298515	0.0398948	0.0287286
64	down	0.0302834	0.036588	0.0382809	0.0347697
144	up	0.0323278	0.033094	0.049306	0.0353601
144	down	0.036647	0.0342221	0.0467166	0.0356278
177	down	0.030047	0.0542221	0.040/100	U.

and interactions among inhomogeneities. These can significantly change local fields, such as the shape of stress curves, maximum angle of stress concentration, and maximum stress concentration value. Our recent work (Wu, Zhang, & Yin, 2023) also studied the stress concentration of one micro-void embedded in a bi-layered structure subjected to mechanical load, which showed even without inhomogeneity interactions, the boundary effects led to an apparent maximum value angle shift.

In the following, Fig. 19 (a-d) plots variations of normal stress along the vertical circumference, and those stress components are compared to that of bimaterial cases (without inhomogeneities) at the same time. Comparing stress curves in Figs. 19 (a-d), it can be noticed that the stress curves for "up" and "down" cases exhibit reverse trends that, which is caused by the definition of angle coordinate θ . For the inhomogeneity in the upper phase, when $\theta = \frac{3\pi}{2}$, the observing point is closest to the bimaterial interface, while $\theta = \frac{\pi}{2}$ is the closest observing point of the inhomogeneity in the lower phase. Comparing maximum values in Fig. 21 (a-d), the inhomogeneity in the lower phase has very slightly greater values; for instance, the maximum value in Fig. 21(d) is 1.88 and 1.93 for the inhomogeneity in the upper and lower phase, respectively. Although Figs. 21(a-d) exhibit similar stress variation, the angle for maximum value are different. For inhomogeneities in the upper phase, $\theta = \pi, 0, 0, \pi$ and for inhomogeneities in the lower phase, $\theta = \pi, 0, 0, \pi$. Notice that for Fig. 19(d), there exists an obvious difference when $\theta \in [0, 0.25]\pi$ for the upper phase and $\theta \in [1.75, 2]\pi$ for the lower phase, which is caused by boundary effects.

Fig. 20 (a-d) plots variations of tangential stress along the vertical circumference, compared with bimaterial cases. In addition to the description in the previous paragraph, the differences among curves "up" and "down" become more apparent. Although the maximum value of stresses in Fig. 20 (a-c) are close, it increases from 1.36 to 1.74 for the upper inhomogeneity and 1.42 to 1.47 for the lower inhomogeneity. The closest observing point of the fourth inhomogeneity to the boundary exists when $\theta=0$ for inhomogeneities in the upper or lower phase. The boundary effects significantly change the local fields and the angle for maximum values are: (i) $\theta=0,0,0,\frac{\pi}{2}$ for the upper inhomogeneity and (ii) $\theta=\frac{\pi}{2}$ for the lower inhomogeneity. Comparing the maximum value of bimaterial cases, an initial conclusion can be drawn that inhomogeneities cause more local stress concentrations.

Figs. 21 (a-d) plot variations of normal stress along the horizontal circumference. It can observed that stress curves on horizontal circumference are not symmetric to $\theta = \pi$, which is caused by the non-symmetric position of the inhomogeneity. Although the

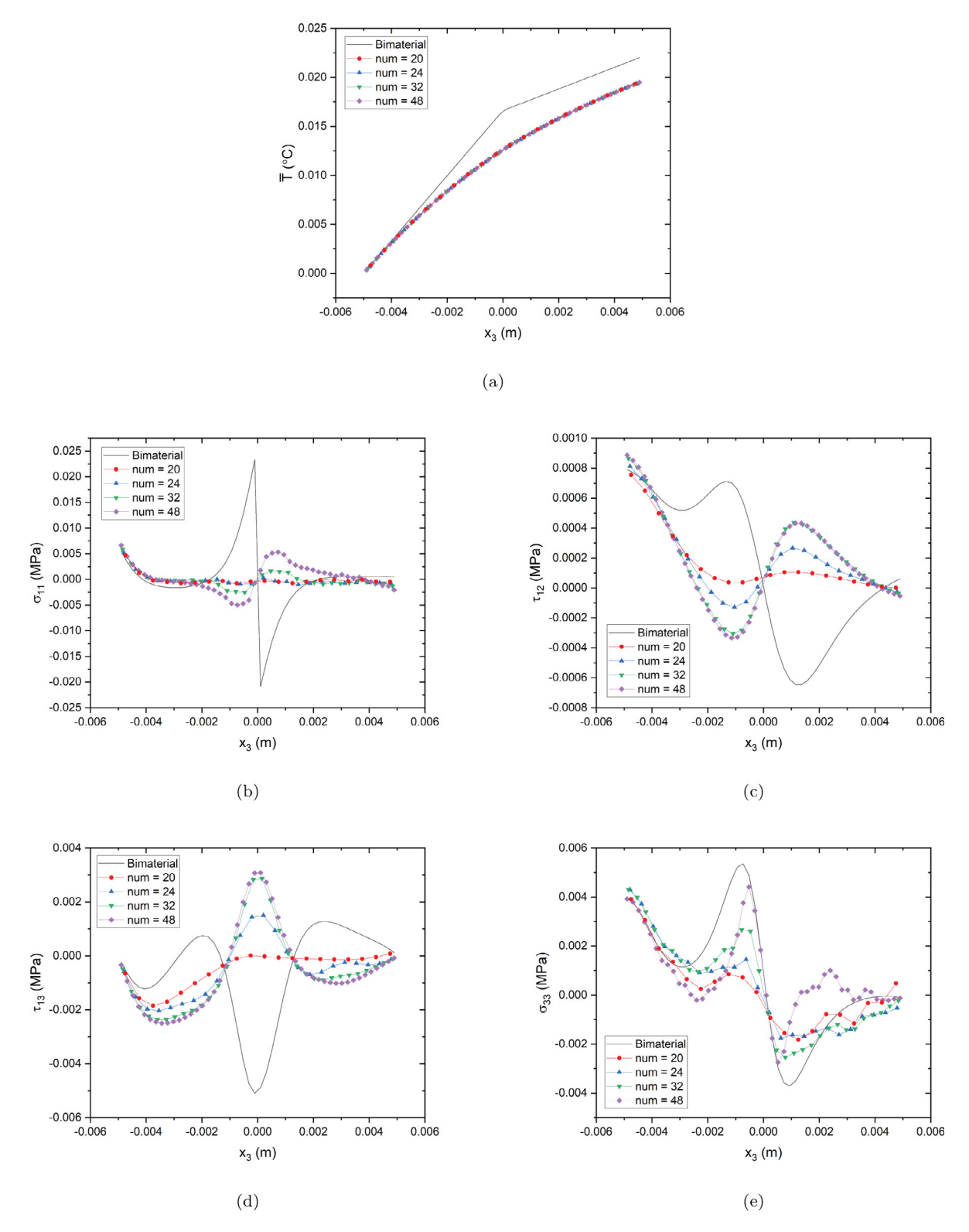


Fig. 17. Variation and comparison of averaged temperature and thermal stresses of four numbers of height division for gradation (20, 24, 32 and 48) subjected to 100 W/m^2 heat flux on the top surface, (a) \overline{T} , (b) σ_{11} , (c) τ_{12} , (d) τ_{13} and (e) σ_{33} .

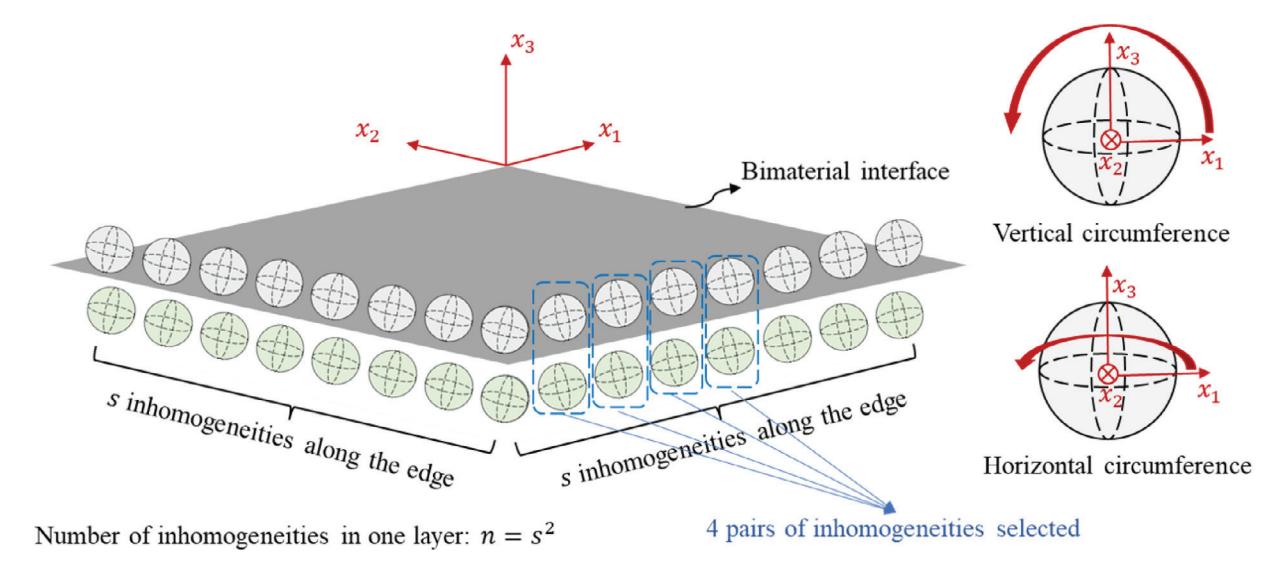


Fig. 18. Schematic illustration of two adjacent layers near the bimaterial interface in the quarter of the FGM composite with two symmetric surfaces; $n = s^2$ spherical inhomogeneities are uniformly distributed in each layer, where n = 25, 36, 64, 144 for num = 20, 24, 32 and 48, respectively; and 4 pairs of inhomogeneities (close to boundary) are selected to plot stress variation along the vertical $(x_1 - x_3)$ and horizontal $(x_1 - x_2)$ circumference.

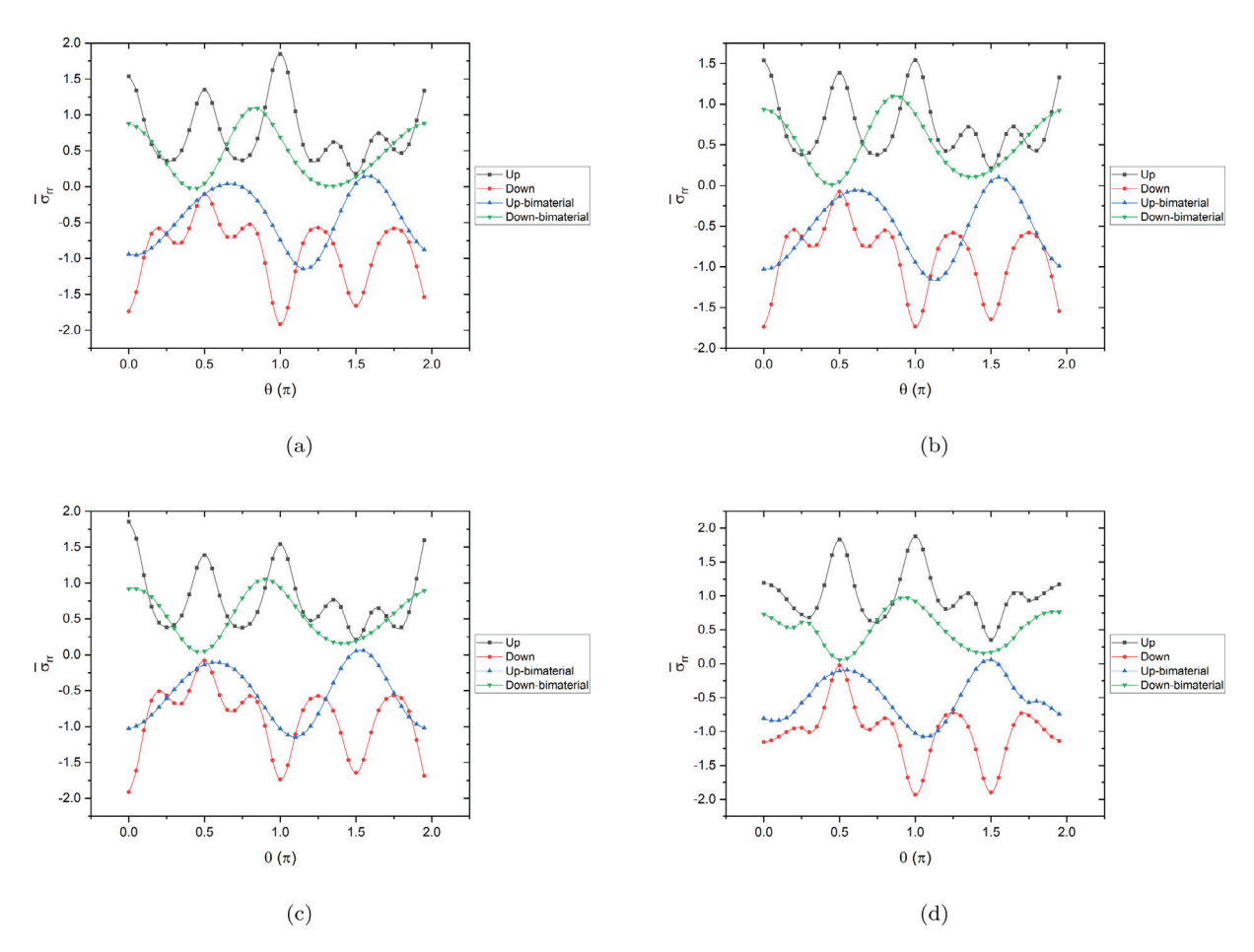


Fig. 19. Variation and comparison of normalized stress $\overline{\sigma}_{rr}$ with bimaterial cases along the vertical circumference for inhomogeneities of adjacent layers when num = 20, (a) the first; (ii) the second; (iii) the third; and (iv) the fourth inhomogeneity along x_2 direction.

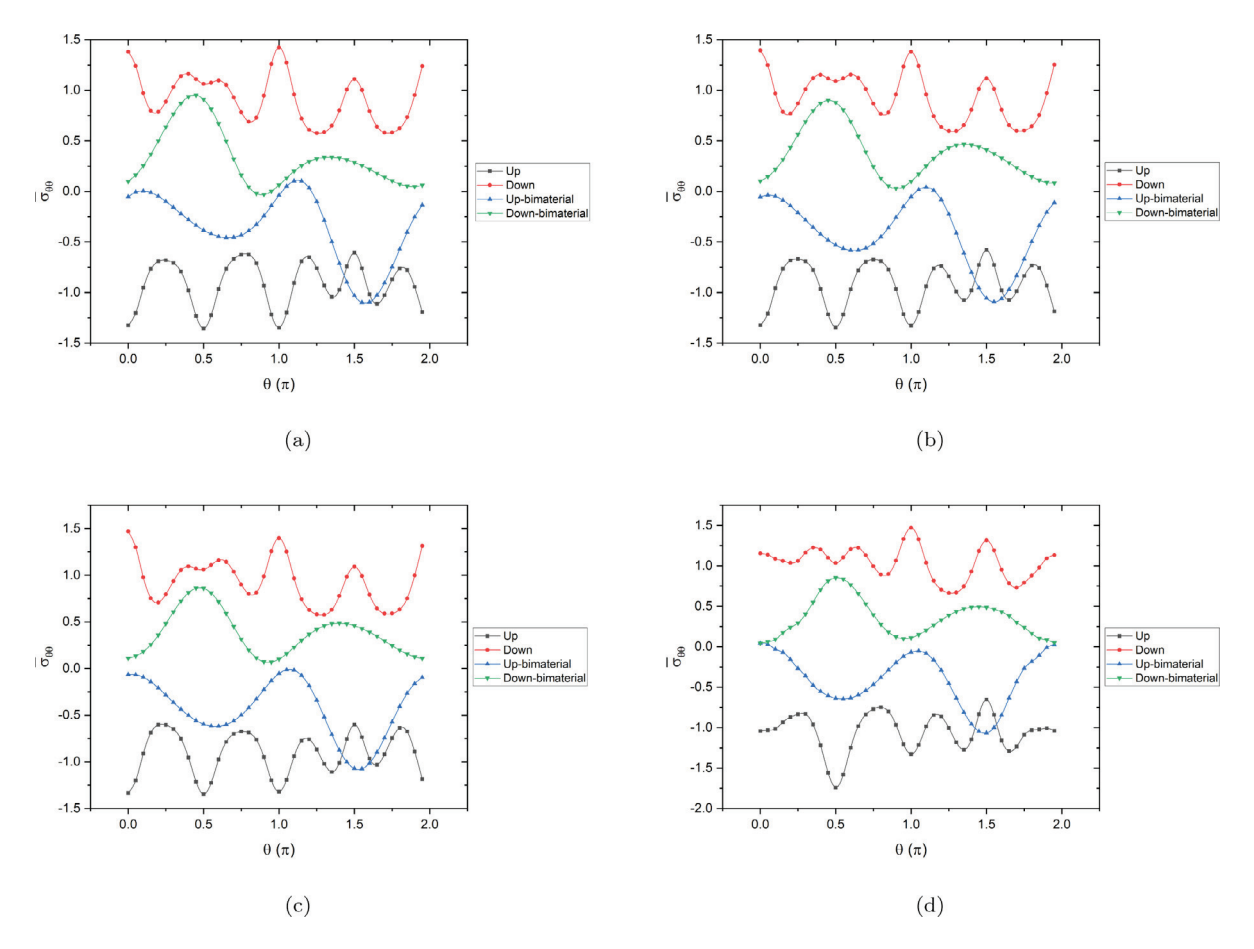


Fig. 20. Variation and comparison of normalized stress $\bar{\sigma}_{\theta\theta}$ with bimaterial cases along the vertical circumference for inhomogeneities of adjacent layers when num = 20, (a) the first; (ii) the second; (iii) the third; and (iv) the fourth inhomogeneity along x_2 direction.

stress values for inhomogeneities in the upper and lower phases may differ, the shapes (distribution) of stress curves are similar. The maximum value appears at the same angle for inhomogeneities in two phases. Specifically, $\theta = \pi$, $\frac{3\pi}{4}$, 0 and $\frac{3\pi}{4}$ for Fig. 21 (a-d), respectively. As discussed previously, due to more intensive boundary effects of the fourth pair of inhomogeneities, stress curves Fig. 21(d) exhibit different trends. Due to the complexity of several coupled factors, explicitly explaining the angle shift of maximum values is challenging. Fig. 22 (a-d) plot variations of tangential stress along the horizontal circumference. Similar to normal stress, the angle of maximum values appears at the same angle as that of normal stress for both upper and lower cases. Compared to the stress curves of bimaterial cases, the variation of stress of horizontal circumference is much smaller than that of vertical ones. However, due to inhomogeneities, the local fields have been significantly disturbed, and fluctuations can be observed.

Figs. 23 (a-d) and Fig. 24 (a-d) plot variations of normal and tangential stresses along the vertical circumference, respectively. Those figures' Stress curves share similar trends as the case *num* = 20. Perhaps the major difference is that the first inhomogeneity is subjected to more intensive boundary effects than the other three. Due to such effects, local fields have been changed significantly that the maximum values in Fig. 23 (a-d) are 5.18, 1.48, 1.02, and 0.92 for the upper case and 3.55, 1.14, 1.06 and 0.86 for the lower case. For tangential stress in Figs. 24 (a-d), the maximum values are 1.42, 0.82, 0.85, and 0.86 for the upper case and 1.72, 1.69, 1.46, and 1.41. Notice that the boundary effects can be obtained in stress curves as bimaterial cases, and Fig. 25(a) and Fig. 26(a) show completely different stress variations and such boundary effects can be measured as the distance from observing points to the boundary. Figs. 25 (a-d) and Fig. 26 (a-d) plot variations of normal and tangential stresses along the horizontal circumference, respectively. Similar phenomena can be observed, with the maximum values 3.39, 0.97, 0.67, and 0.63 for the upper case and 2.79, 0.90, 0.83, and 0.82 for the lower case in Figs. 25 (a-d). Moreover, the maximum values are 1.35, 0.71, 0.74, and 0.75 for the upper case and 1.23, 1.21, 1.08, and 1.14 for the lower case in Figs. 26 (a-d). Although stress concentration becomes more severe for inhomogeneities close to the boundary, the maximum stress for interior inhomogeneities becomes smaller.

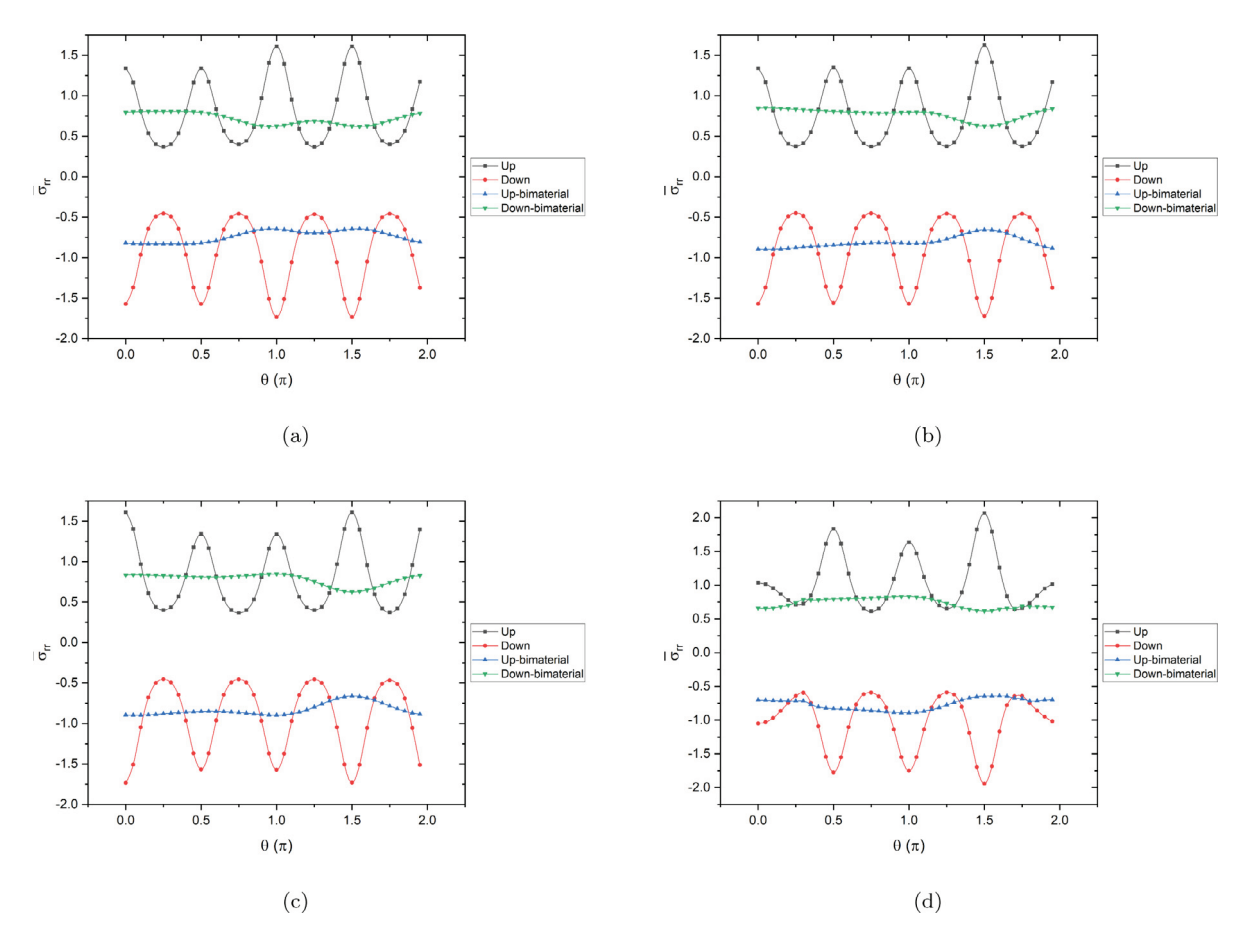


Fig. 21. Variation and comparison of normalized stress $\bar{\sigma}_{rr}$ with bimaterial cases along the horizontal circumference for inhomogeneities of adjacent layers when num = 20, (a) the first; (ii) the second; (iii) the third; and (iv) the fourth inhomogeneity along x_2 direction.

6. Conclusions

This paper extends the single-domain iBEM algorithm to efficiently simulate three-dimensional thermoelastic problems for a bi-layered system containing multiple inhomogeneities. The accuracy of this method is verified by the FEM simulation considering inhomogeneities with bimaterial interfacial effects and interactions with other inhomogeneities. The present method exhibits much higher efficiency than the FEM in mesh discretization, storage, and computational costs, and thus enables the simulation of a bi-phase FGM containing > 10.000 particles with the following uniqueness features:

- 1. The iBEM converts the former complicated volume integral of temperature and kernel functions to boundary integrals of the thermoelastic fundamental solution and Eshelby's tensors of inhomogeneities only, which significantly reduce volume-integral related computational costs and resources.
- 2. Using the bi-matrix model to simulate functionally graded materials by interchanging inhomogeneities and two matrices further reduces computational costs on simulation of inhomogeneities in the one-matrix model (saving half costs on simulation of inhumanities for linear gradation). This algorithm is suitable and stable for thermoelastic modeling of bi-layered composite and FGMs.
- 3. Using the bimaterial fundamental solution analytically address the interfacial continuity between material layers and significantly increases the robustness and convergence of the numerical methods.
- 4. The DEIM assembles the coupled linear equation system of temperature and displacement in one step, and improves the accuracy and efficiency compared with the two-step thermomechanical analysis with temperature field solved separately.
- 5. The high efficient iBEM algorithm enables the cross-scale modeling of FGM samples with high fidelity microstructure for digital twins of material testing.

Overall, this method provides a powerful tool for the design and analysis of FGMS, and can be extended to multiphysical and multiscale modeling of other composite materials.

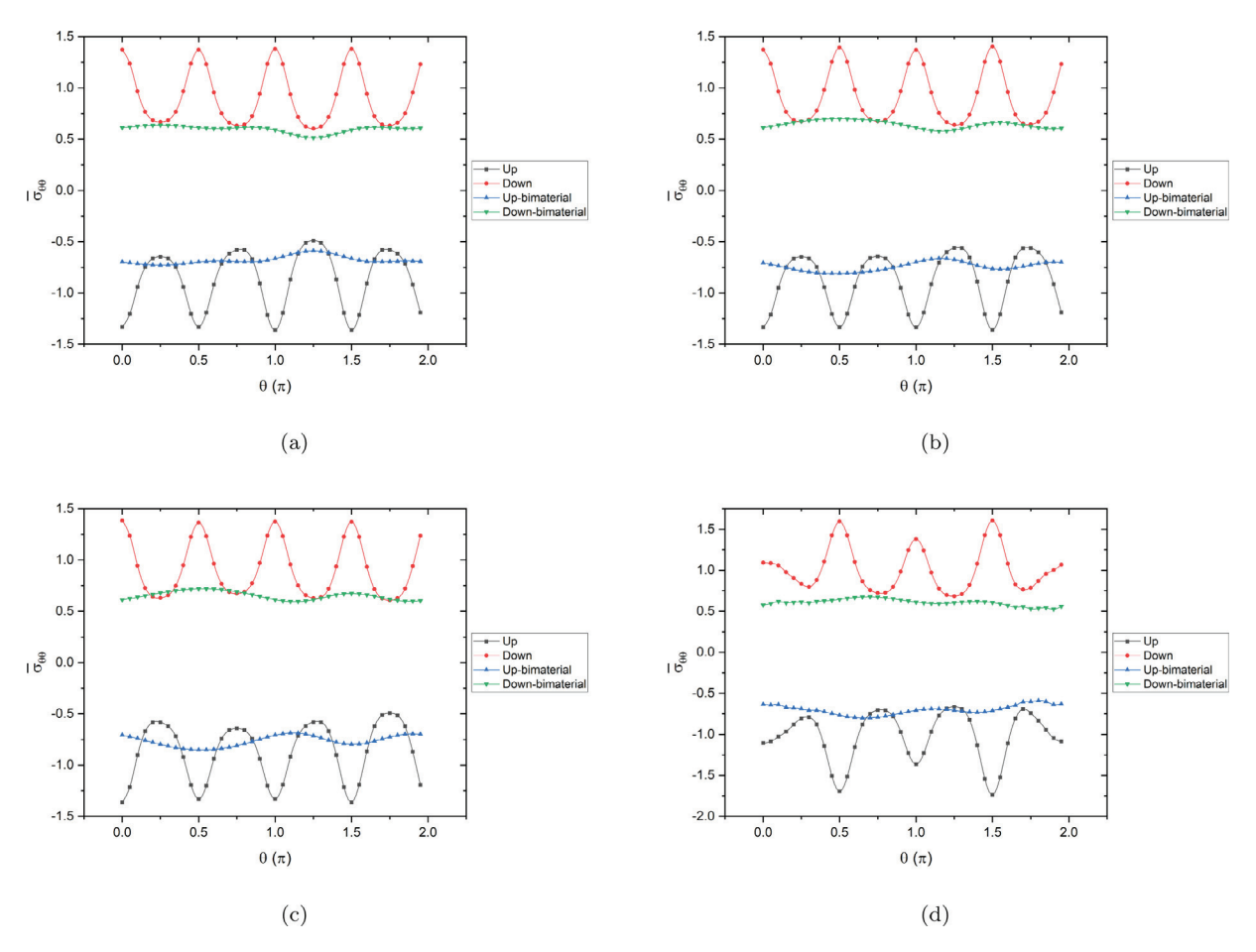


Fig. 22. Variation and comparison of normalized stress $\bar{\sigma}_{\theta\theta}$ with bimaterial cases along the horizontal circumference for inhomogeneities of adjacent layers when num = 20, (a) the first; (ii) the second; (iii) the third; and (iv) the fourth inhomogeneity along x_2 direction.

CRediT authorship contribution statement

Chunlin Wu: Conceptualization, Data curation, Funding acquisition, Methodology, Software, Validation, Visualization, Writing – original draft. **Liangliang Zhang:** Writing – review & editing. **George J. Weng:** Writing – review & editing. **Huiming Yin:** Funding acquisition, Resources, Supervision, Writing – review & editing.

Declaration of competing interest

The authors declare that they have no known competing financial interests or personal relationships that could have appeared to influence the work reported in this paper.

Data availability

Data will be made available on request.

Acknowledgments

This work is sponsored by the National Natural Science Foundation of China No. 12102458 and No. 12302086 and National Science Foundation IIP #1941244, U.S. Department of Agriculture NIFA #2021-67021-34201, whose support is gratefully acknowledged.

Appendix A. Supplementary data

Supplementary material related to this article can be found online at https://doi.org/10.1016/j.ijengsci.2024.104040.The supplemental materials aim to provide more information on stress concentrations along the vertical and horizontal circumferences when height divisions are num = 24 and num = 32. The averaged stress components have been provided in the Table 5.

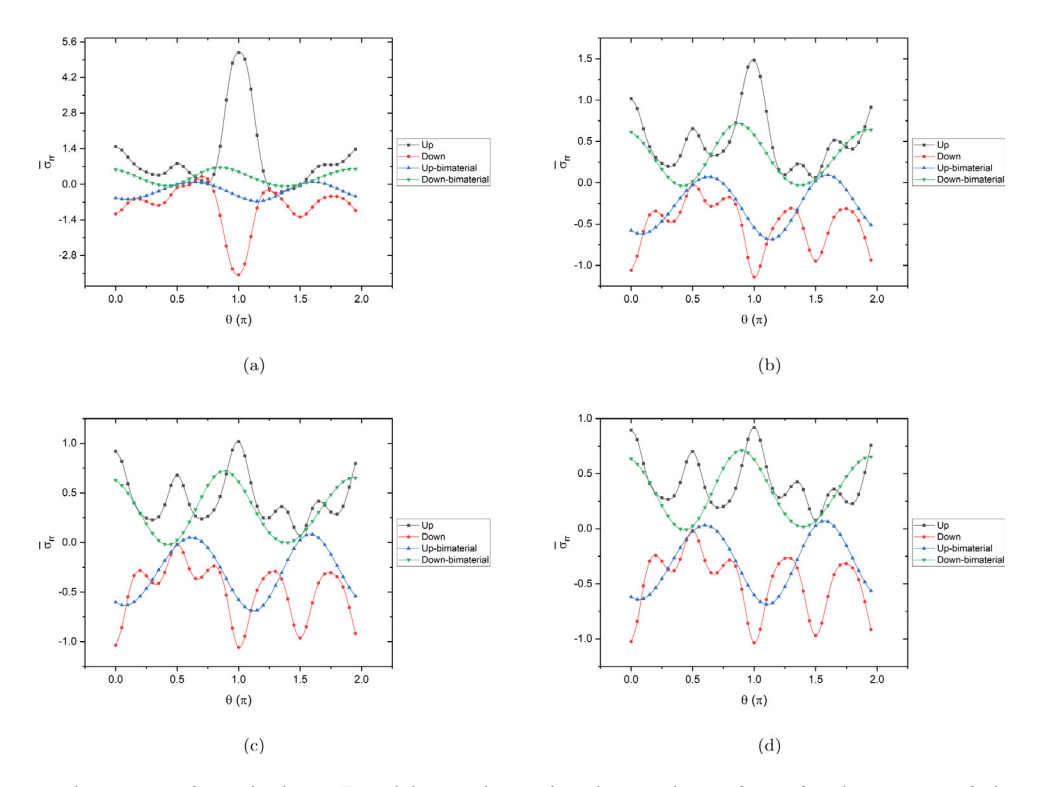


Fig. 23. Variation and comparison of normalized stress $\overline{\sigma}_{rr}$ with bimaterial cases along the vertical circumference for inhomogeneities of adjacent layers when num = 48, (a) the first; (ii) the second; (iii) the third; and (iv) the fourth inhomogeneity along x_2 direction.

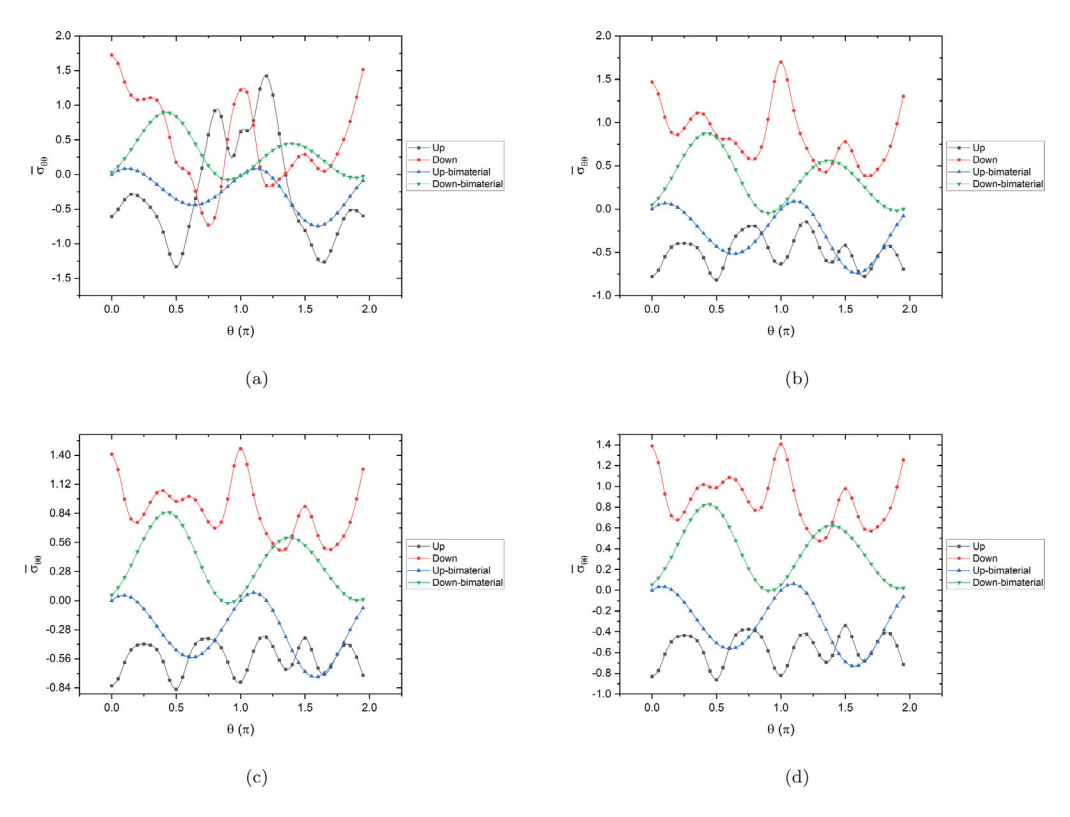


Fig. 24. Variation and comparison of normalized stress $\overline{\sigma}_{\theta\theta}$ with bimaterial cases along the vertical circumference for inhomogeneities of adjacent layers when num = 48, (a) the first; (ii) the second; (iii) the third; and (iv) the fourth inhomogeneity along x_2 direction.

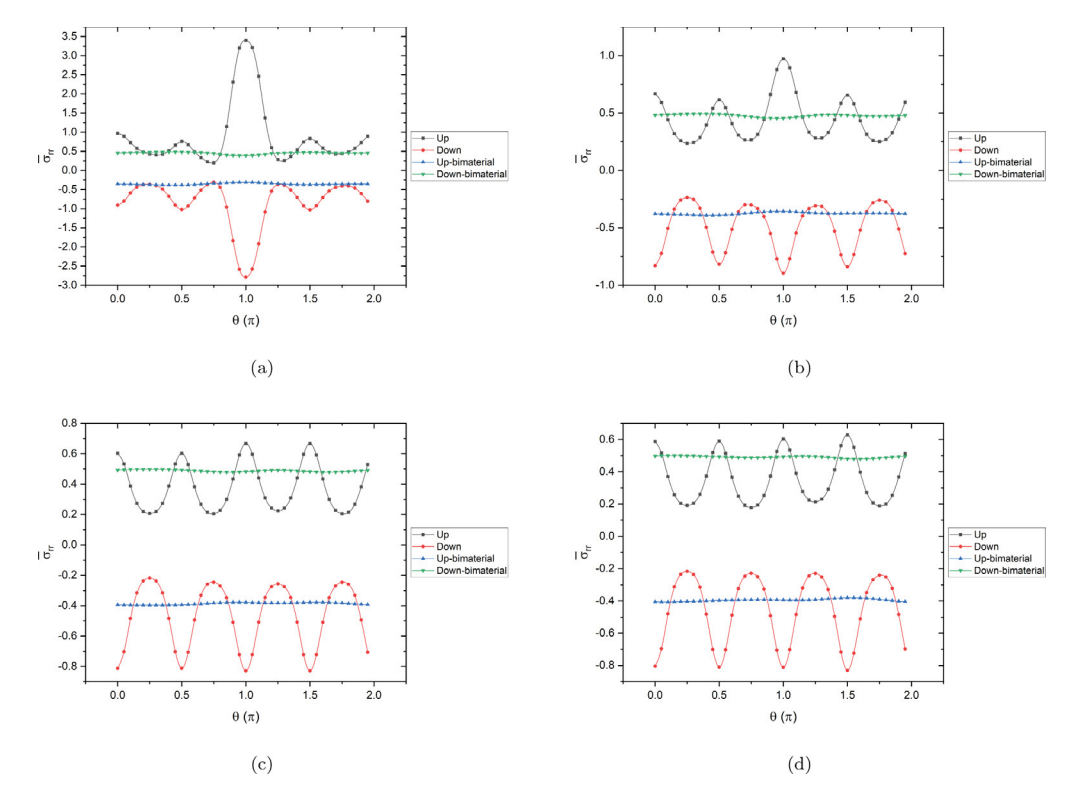


Fig. 25. Variation and comparison of normalized stress $\overline{\sigma}_{rr}$ with bimaterial cases along the horizontal circumference for inhomogeneities of adjacent layers when num = 48, (a) the first; (ii) the second; (iii) the third; and (iv) the fourth inhomogeneity along x_2 direction.

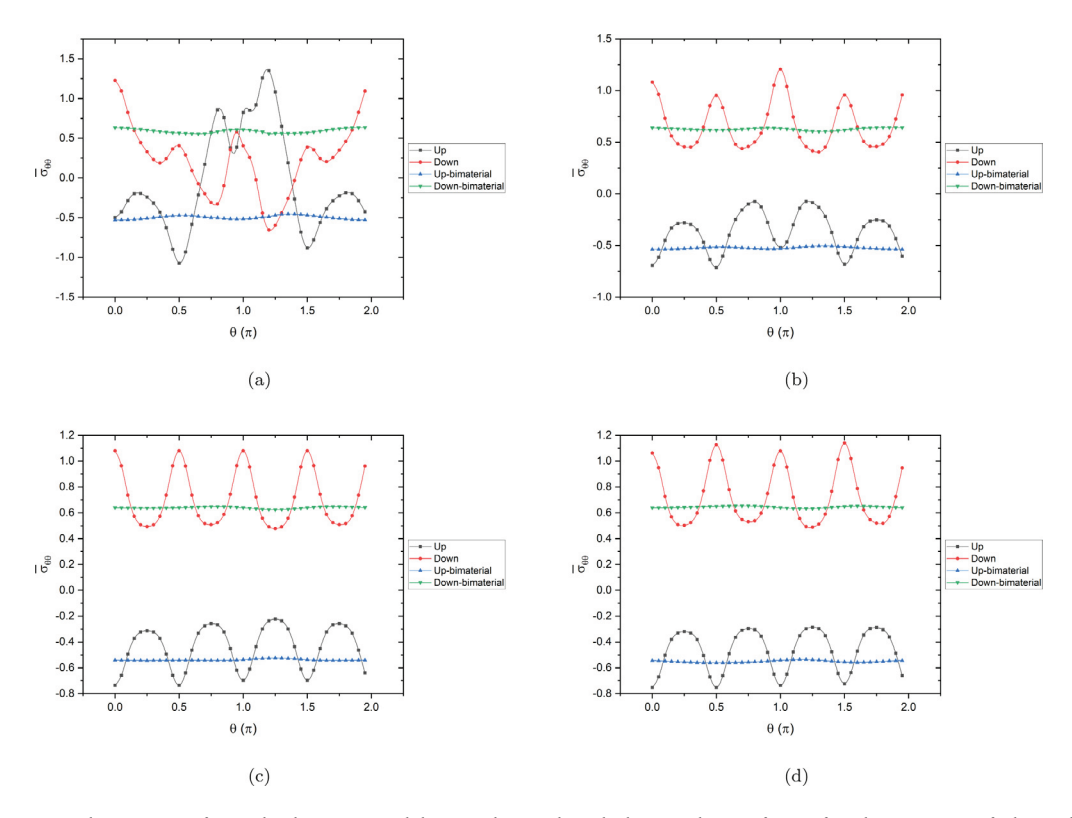


Fig. 26. Variation and comparison of normalized stress $\bar{\sigma}_{\theta\theta}$ with bimaterial cases along the horizontal circumference for inhomogeneities of adjacent layers when num = 48, (a) the first; (ii) the second; (iii) the third; and (iv) the fourth inhomogeneity along x_2 direction.

References

- Aboudi, J., Pindera, M.-J., & Arnold, S. M. (1996a). Thermo plasticity theory for bidirectionally functionally graded materials. *Journal of Thermal Stresses*, 19(9), 809–861
- Aboudi, J., Pindera, M.-J., & Arnold, S. M. (1996b). Thermoelastic theory for the response of materials functionally graded in two directions. *International Journal of Solids and Structures*, 33(7), 931–966.
- Aboudi, J., Pindera, M.-J., & Arnold, S. (1999). Higher-order theory for functionally graded materials. Composites Part B (Engineering), 30(8), 777-832.
- Agrawal, P., Conlon, K., Bowman, K., Sun, C., Cichocki, F., & Trumble, K. (2003). Thermal residual stresses in co-continuous composites. Acta Materialia, 51(4), 1142–1156
- Anlas, G., Santare, M., & Lambros, J. (2000). Numerical calculation of stress intensity factors in functionally graded materials. *International Journal of Fracture*, 104(2), 131–143.
- Barber, J. (1992). Elasticity. Dordrecht: Springer Dordrecht.
- Boussinesq, J. (1885). Applications des potentiels à l'étude de l'équilibre et du mouvement des solides élastiques. Gauthier-Villars.
- Burlayenko, V., Altenbach, H., Sadowski, T., Dimitrova, S., & Bhaskar, A. (2017). Modelling functionally graded materials in heat transfer and thermal stress analysis by means of graded finite elements. *Applied Mathematical Modelling*, 45, 422–438.
- Carvalho, O., Buciumeanu, M., Madeira, S., Soares, D., Silva, F., & Miranda, G. (2015). Optimization of AlSi-CNTs functionally graded material composites for engine piston rings. *Materials & Design*, 80, 163–173.
- Chawla, K. K. (2003). Ceramic matrix composites. Springer US.
- Ebrahimijahan, A., Dehghan, M., & Abbaszadeh, M. (2022). Simulation of plane elastostatic equations of anisotropic functionally graded materials by integrated radial basis function based on finite difference approach. *Engineering Analysis with Boundary Elements*, 134, 553–570.
- Eshelby, J. D. (1957). The determination of the elastic field of an ellipsoidal inclusion, and related problems. *Proceedings of the Royal Society of London. Series A. Mathematical and Physical Sciences*, 241(1226), 376–396.
- Eshelby, J. D. (1959). The elastic field outside an ellipsoidal inclusion. Proceedings of the Royal Society of London. Series A. Mathematical and Physical Sciences, 252(1271), 561–569.
- Fujimoto, T., & Noda, N. (2004). Influence of the compositional profile of functionally graded material on the crack path under thermal shock. *Journal of the American Ceramic Society*, 84(7), 1480–1486.
- Hatta, H., & Taya, M. (1986). Equivalent inclusion method for steady state heat conduction in composites. *International Journal of Engineering Science*, 24, 1159–1170.
- Hou, P.-F., Li, Q.-H., & Jiang, H.-Y. (2013). Three-dimensional steady-state general solution for isotropic thermoelastic materials with applications II: Green's functions for two-phase infinite body. *Journal of Thermal Stresses*, 36(8), 851–867.
- Jha, D., Kant, T., & Singh, R. (2013). A critical review of recent research on functionally graded plates. Composite Structures, 96, 833-849.
- Kesler, O., Matejicek, J., Sampath, S., Suresh, S., Gnaeupel-Herold, T., Brand, P., & Prask, H. (1998). Measurement of residual stress in plasma-sprayed metallic, ceramic and composite coatings. *Materials Science & Engineering A*, 257(2), 215–224.
- Khor, K., & Gu, Y. (2000). Thermal properties of plasma-sprayed functionally graded thermal barrier coatings. Thin Solid Films, 372(1-2), 104-113.
- Kim, J.-H., & Paulino, G. H. (2002). Isoparametric graded finite elements for nonhomogeneous isotropic and orthotropic materials. *Journal of Applied Mechanics*, 69(4), 502–514.
- Kumar, S., Reddy, K. M., Kumar, A., & Devi, G. R. (2013). Development and characterization of polymer-ceramic continuous fiber reinforced functionally graded composites for aerospace application. *Aerospace Science and Technology*, 26(1), 185–191.
- Lin, Q., Chen, F., & Yin, H. (2017). Experimental and theoretical investigation of the thermo-mechanical deformation of a functionally graded panel. *Engineering Structures*, 138, 17–26.
- Ma, H., Hu, G., Wei, Y., & Liang, L. (2018). Inclusion problem in second gradient elasticity. International Journal of Engineering Science, 132, 60-78.
- Mura, T. (1987). Micromechanics of defects in solids. Dordrecht: Springer Netherlands.
- Prasad, N. N. V., Aliabadi, M. H., & Rooke, D. P. (1994). The dual boundary element method for thermoelastic crack problems. *International Journal of Fracture*, 66(3), 255–272.
- Ram, S., Chattopadhyay, K., & Chakrabarty, I. (2017). High temperature tensile properties of centrifugally cast in-situ Al-Mg2Si functionally graded composites for automotive cylinder block liners. *Journal of Alloys and Compounds*, 724, 84–97.
- Reiter, T., & Dvorak, G. J. (1998). Micromechanical models for graded composite materials: ii. thermomechanical loading. *Journal of the Mechanics and Physics of Solids*, 46(9), 1655–1673.
- Reiter, T., Dvorak, G. J., & Tvergaard, V. (1997). Micromechanical models for graded composite materials. *Journal of the Mechanics and Physics of Solids*, 45(8), 1281–1302.
- Roy, S. (2020). Functionally graded coatings on biomaterials: a critical review. Materials Today Chemistry, 18, Article 100375.
- Saleh, B., Jiang, J., Fathi, R., Al-hababi, T., Xu, Q., Wang, L., Song, D., & Ma, A. (2020). 30 Years of functionally graded materials: An overview of manufacturing methods, applications and future challenges. *Composites Part B (Engineering)*, 201, Article 108376.
- Santare, M. H., & Lambros, J. (2000). Use of graded finite elements to model the behavior of nonhomogeneous materials. *Journal of Applied Mechanics*, 67(4), 819–822.
- Shinohara, Y. (2013). Functionally graded materials. In Handbook of advanced ceramics (pp. 1179-1187). Elsevier.
- Suresh, S., & Mortensen, A. (1997). Functionally graded metals and metal-ceramic composites: Part 2 Thermomechanical behaviour. *International Materials Reviews*, 42(3), 85–116.
- Tanvir, A. N. M., Islam, M. D., & Ahmed, F. (2017). Analysis of thermoelastic characteristics in a thick walled FGM cylinder. In AIP conference proceedings.
- Walpole, L. (1996). An elastic singularity in joined half-spaces. International Journal of Engineering Science, 34(6), 629-638.
- Walpole, L. (1997). An inclusion in one of two joined isotropic elastic half-spaces. IMA Journal of Applied Mathematics, 59(2), 193-209.
- Wang, P., Wang, B., Wang, K., Hirakata, H., & Zhang, C. (2019). Analysis of three-dimensional ellipsoidal inclusions in thermoelectric solids. *International Journal of Engineering Science*, 142, 158–169.
- Wang, T., Wu, C., Zhang, L., & Yin, H. (2022). The Green's function-based thermal analysis of a spherical geothermal tank in a semi-infinite domain. *Journal of Applied Mechanics*, 89(7), Article 071008.
- Wu, C., Wang, T., & Yin, H. (2023). The Green's function based thermoelastic analysis of spherical geothermal tanks in a semi-infinite domain. *Journal of the Mechanics and Physics of Solids*, 173, Article 105207.
- Wu, C., Zhang, L., Cui, J., & Yin, H. (2023). Three-dimensional elastic analysis of a bi-material system with a single domain boundary element method. *Engineering Analysis with Boundary Elements*, 146, 17–33.
- Wu, C., Zhang, L., Singhatanadgid, P., & Zhang, D. (2023). Thermoelastic analysis of a bi-layered system with the single domain inclusion-based boundary element method. *Engineering Analysis with Boundary Elements*, 157, 374–389.
- Wu, C., Zhang, L., & Yin, H. (2023). Stress concentration of a microvoid embedded in a bilayered material considering the boundary effects. *Journal of Engineering Mechanics*, 149(2).

- Yin, H., Paulino, G., Buttlar, W., & Sun, L. (2007). Micromechanics-based thermoelastic model for functionally graded particulate materials with particle interactions. *Journal of the Mechanics and Physics of Solids*, 55(1), 132–160.
- Yin, H., Song, G., Zhang, L., & Wu, C. (2022). The inclusion-based boundary element method. Academic Press.
- Yin, H., Sun, L., & Paulino, G. H. (2004). Micromechanics-based elastic model for functionally graded materials with particle interactions. *Acta Materialia*, 52(12), 3535–3543.
- Zou, W.-N., & He, Q.-C. (2018). Revisiting the problem of a 2D infinite elastic isotropic medium with a rigid inclusion or a cavity. *International Journal of Engineering Science*, 126, 68–96.